FERMILAB-FN-1119-AD
CERN-ACC-NOTE-2021-0010

24 March 2021
michael.hofer@cern.ch

Nonlinear optics measurements in IOTA

M. Hofer and R. Tomás
CERN, CH-1211 Geneva, Switzerland
A. Romanov, G. Stancari, A. Valishev
Fermi National Laboratory, Batavia, IL 60510, USA
N. Kuklev
The University of Chicago, Department of Physics, Chicago, IL 60637, USA
S. Szustkowski
Northern Illinois University, DeKalb, IL 60115, USA

Abstract

Nonlinear integrable optics is a recently proposed accelerator lattice design approach which allows to generate an amplitude dependent tune shift which is needed in high brightness accelerators to mitigate fast coherent instabilities. Whereas usually octupoles are used to achieve this task, this concept allows doing so without exciting any resonances, in turn preventing any particle loss. The concept is based around a special magnet design, together with specific constraints on the optics of the accelerator. To study such a system, the Integrable Optics Test Accelerator (IOTA) was recently constructed and commissioned at Fermilab. For the assessment of the performance of this concept, good knowledge of the optics and the (non-)linear dynamics without the special magnet is of key importance. As such, measurements were conducted in the IOTA ring, using the captured turn-by-turn data by the beam position monitors after excitation to infer quantities such as amplitude detuning and resonance driving terms. In this note, first results of these measurements are presented.

This document was prepared by IOTA collaboration using the resources of the Fermi National Accelerator Laboratory (Fermilab), a U.S. Department of Energy, Office of Science, HEP User Facility. Fermilab is managed by Fermi Research Alliance, LLC (FRA), acting under Contract No. DE-AC02-07CH11359.

Contents

1 Introduction

In order to push the performance of current and potential future accelerator projects, the assessment of nonlinear beam dynamics has become a mainstay in the design and commissioning in these machines. In synchrotrons, nonlinear magnetic elements may have a detrimental impact on the machine performance due to for example excitation of strong resonances and reduction of dynamic aperture. As such, care is taken already in the design phase of many machines to evaluate the impact of higher order multipoles to define feasible correction strategies [1]. Once a machine is set up and running, it is equally important to check the validity of the prior models through dedicated measurements to ensure thorough understanding of involved dynamics in the accelerator and as solid starting point for machine tuning. A variety of measurement techniques are available to identify specific error sources, which can be conducted either via beam-based methods such as assessing feed-down effects via closed orbit modifications [2, 3] or based on turn-by-turn data [4], which was the method of choice for the studies presented in this note.

By performing spectral analysis on the turn-by-turn motion of a transversally excited particle bunch, not only the main spectral lines (corresponding to the tunes) may be observed but also higher order lines. These spectral lines, associated with specific resonances, are then used to determine the distortion of the phase-space compared to the ideal linear case due to those resonances via the resonance driving term (RDT) formalism. The evolution of amplitude of specific RDTs around the accelerator ring also allows to assess location and strength of nonlinear magnets [5].

The study of the nonlinear dynamics and assessment of nonlinear magnetic fields is of particular interest in accelerators based on the concept of nonlinear integrable optics [6]. Here, by using a magnet with a particular magnetic field shape, particles experience specific nonlinear effects such as amplitude detuning while in the ideal case no resonances are excited, in turn preventing any particle loss. The feasibility of this concept is currently being tested at the

Integrable Optics Test Accelerator (IOTA) at Fermilab [7].

The presented concept to achieve nonlinear integrable optics imposes strict constraints on the accelerator characteristics, such as equal tunes in both planes $Q_x = Q_y$, layout, and in particular also on dynamics outside of the section where the NL-magnet is located. Specifically, a linear transfer map is assumed between the ends of this straight section in the original derivations, which due to the presence of chromaticity sextupoles or potential field errors is not the case in the IOTA accelerator. Given these specific constraints on the optics and the general goal of the demonstration of nonlinear integrable optics, an assessment of sources of nonlinear magnetic fields is thus important for this feasibility study, further potentially allowing to clearly attribute particle loss to of specific sources.

The aim of this note is to present a first look into the nonlinear dynamics of the IOTA accelerator, generated by elements other than the dedicated nonlinear channels. The experiments were carried out in March 2020 during IOTA Run 2. In Sec. 2, a brief introduction to the concept of nonlinear integrable optics is presented, aiming to motivate why the knowledge and control of nonlinear magnets is critical here. An overview over the IOTA accelerator is then presented in the following Sec 3. Here, focus will be put on hardware and operational aspects relevant for the conducted experiments and results, which will be presented in Sec 4.

2 Nonlinear integrable optics

In modern synchrotrons, the use of nonlinear magnets has become a necessity in order to achieve the ever increasing performance goals while itself also possibly posing a limiting factor. One such example would be the necessity to use octupole magnets in the LHC to suppress collective instabilities via Landau damping due to an amplitude-dependant tune-spread while these also excite resonances which may lead to particle loss. As such, a trade-off has to be found between the stabilizing effect of the generated amplitude detuning and the excitation of resonances with an associated negative impact on the dynamic aperture (DA), which is the maximum amplitude up to which bounded motion of the particles for a given time span occurs.

To overcome the problem of the particle loss associated with nonlinear magnetic fields and associated resonances, in [6] a novel approach is discussed to find a nonlinear system with integrable motion which is feasible to be implemented in a particle accelerator. A fully integrable system is characterized by regular bounded motion of particles independent of their initial conditions or, conversely, a system with same number of conserved quantities as degrees of freedom, which for a 4D system requires two invariants. An accelerator can be described by a Hamiltonian as

$$H = \frac{p_x^2}{2} + \frac{p_y^2}{2} + K(s)\Big(\frac{x^2}{2} + \frac{y^2}{2}\Big) + V(x, y, s) \ , \tag{1}$$

where $K(s)$ represents the linear focusing component and $V(x, y, s)$ an $s-$dependent nonlinear potential. In order to find a system with two invariants of motion which can be can

be achieved with magnets, the system is moved from an s-dependent system to a system dependent on the phase ψ, which is then expressed in normalized coordinates

$$z_N = \frac{z}{\sqrt{\beta_z(s)}},\ p_N = p\sqrt{\beta_z(s)} - \frac{\beta_z'(s)}{2\sqrt{\beta_z(s)}},\ z \in \{x, y\}\ . \tag{2}$$

The Hamiltonian then takes the following form

$$H_N = \frac{p_{x_N}^2 + p_{y_N}^2}{2} + \frac{x_N^2 + y_N^2}{2} + U(x_N, y_N)\ , \tag{3}$$

with the specific potential

$$U(x_N, y_N) = \beta(\psi) V\Big(x_N\sqrt{\beta(\psi)}, y_N\sqrt{\beta(\psi)}, s(\psi)\Big) \tag{4}$$

to be found which may yield a second invariant next to the time-independent Hamilton from Eq. (3) itself. In [6], families of solutions for different coordinate systems are presented, most notably for elliptic coordinates

$$\xi = \frac{\sqrt{(x+c)^2 + y^2} + \sqrt{(x-c)^2 + y^2}}{2c}\ , \tag{5}$$

$$\eta = \frac{\sqrt{(x+c)^2 + y^2} - \sqrt{(x-c)^2 + y^2}}{2c}\ , \tag{6}$$

where a potential of the form

$$U(x_n, y_n) = \frac{f(\xi) + g(\eta)}{\xi^2 - \eta^2} \tag{7}$$

with f and g defined as

$$f(\xi) = \xi\sqrt{\xi^2 - 1}\Big[d + t\cosh^{-1}(\xi)\Big]\ , \tag{8}$$

$$g(\eta) = \eta\sqrt{1 - \eta^2}\Big[b + t\cos^{-1}(\eta)\Big]\ , \tag{9}$$

which allow realization using magnetic fields given that this potential also satisfies the Laplace Equation. The form of the Hamilton of Eq. (1) with the axial symmetric focusing imposes some constraint on the lattice design. One potential solution is displayed in Fig. 1, where the lattice is split into two parts, a drift-space of length L with equal β-functions in both planes and where the special nonlinear potential is installed and a so called T-insert, being a linear transfer-map.

In turn, also the choice of the working point of the accelerator is limited to $Q_x = Q_y$. Implementing such a system in an accelerator would lead to generation of a tune spread whilst not exciting any resonances, in turn avoiding any particle loss and thus overcoming potential performance limitations due to coherent instabilities.

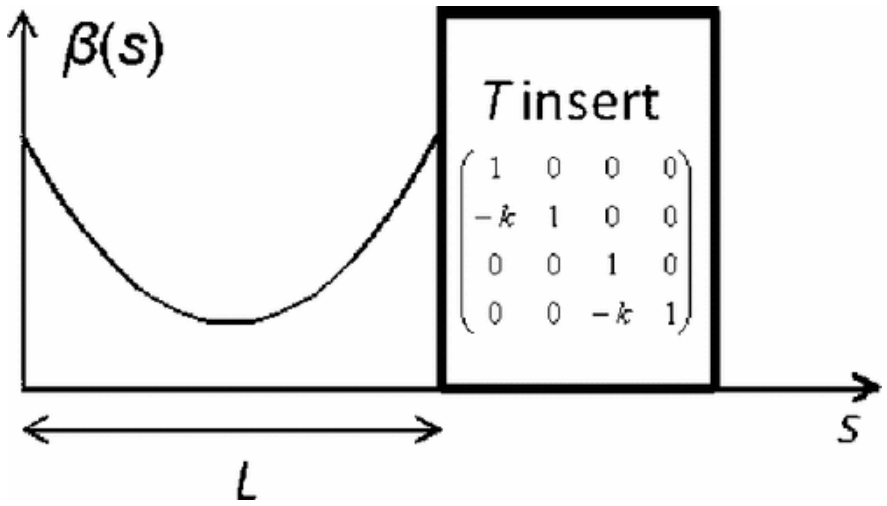

Figure 1: Schematic illustration of a lattice required to provide nonlinear integrable motion as described in [6].

However, effects such as chromaticity may lead to a violation of the imposed constraints, in turn restricting any beneficial effects to particles within a limited momentum deviation range. In [8], it was shown that a chromaticity correction using sextupoles can restore integrability for off-momentum particles. This however violates the aforementioned constraint of the linear transfer-map outside of the nonlinear channel and in turn resonances will be excited. Similarly so, nonlinear magnetic field imperfections may add to this.

Furthermore, as presented in [9], it can be shown that the first term of the multipole expansion of the potential in Eq. (7) for a given set of parameters b and d represents a quadrupole. As such, the powering of the NL-magnet will entail a change of the tunes, as illustrated in Fig. 2. As such, the choice of the working point, or conversely the strength t of the NL-magnet, may be limited due to the two sextupole resonances in the vicinity of the tune curve. Similarly so, even for working points sufficiently far away from those resonances, due to the significant amplitude detuning created by the NL-magnet, these resonances might be approached by particles and may lead to a subsequent particle loss. Depending on the number of allowed particle losses, the impact of these resonances could thus be a limiting factor for the created tune spread.

Due to the aforementioned arguments, the identification of nonlinear elements in an accelerator lattice built around the concept of nonlinear integrable optics, characterisation of critical resonances and possible optimization of any powering or correction scheme to reduce the resonance strength may thus assist in restoring near-integrability of the nonlinear motion and reducing particle loss.

3 The IOTA accelerator

One of the first accelerators built around the concept of nonlinear integrable optics is the Integrable Optics Test Accelerator (IOTA) at Fermilab. Housed at Fermilab Accelerator Sci-

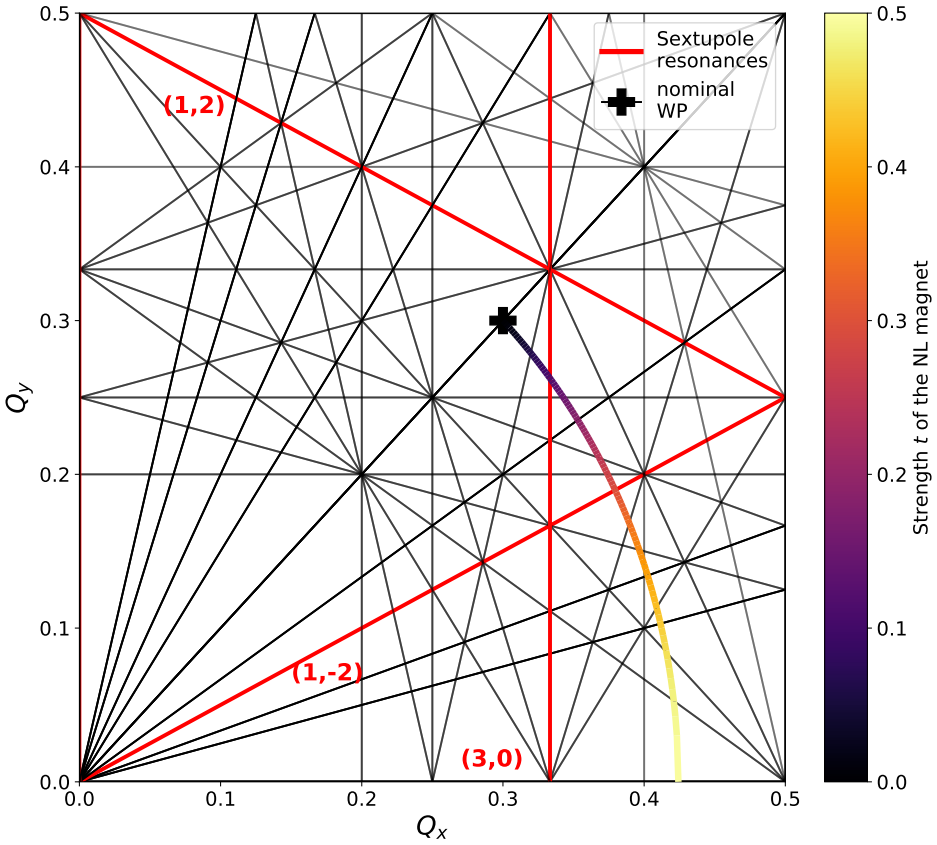

Figure 2: Change of the horizontal/vertical tune during different strengths t of the NL-magnet and resonances up to fifth order. Marked in red are normal sextupole resonances. The working point of the bare lattice with the NL-magnet depowered was assumed to be $Q_{x,y} = 5.30$.

ence and Technology (FAST) facility, the storage ring with a circumference of 40 m, together with the already established superconducting FAST linac and the proton injector currently in development, allows not only for studies on nonlinear integrable optics but also, amongst others, demonstration of optical stochastic cooling and experiments with electron lenses. A comprehensive overview over the facility can be found in [7]. In the following, only a brief overview of the characteristics of the IOTA storage ring, relevant to the studies presented in the next section, is presented. In Fig. 3, the layout of the accelerator is presented.

It consists of 8 straight sections, separated by dipoles with a bending angle of either 30° or 60°. The straight sections on the top left and top right house the so called octupole string, consisting of 17 individually powered octupoles, and the special nonlinear magnet, implementing a potential as described in Eq. (7), respectively. The beam is injected in the center straight on the top, which is also where the horizontal and vertical kicker [10] are located, used to bring the injected beam on the closed orbit or excite the particle bunch transversally. During Run II, in total 4 sextupoles were used to correct chromaticity in the ring, 2 in each of the short straight sections, located in between the 60° dipoles. The sextupoles in the same straight section are separated by a phase advance of $0.06 \cdot 2\pi$ $[rad]$

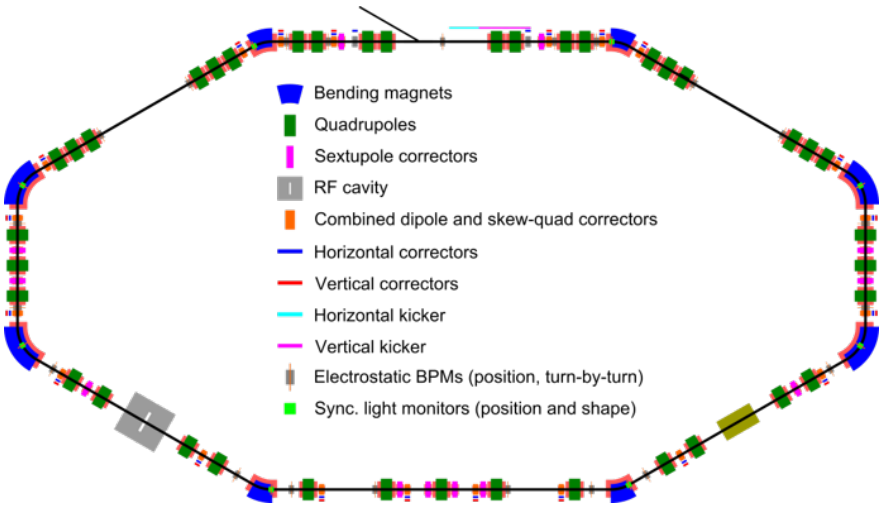

Figure 3: Layout of the IOTA ring.

in the horizontal and $0.25 \cdot 2\pi$ $[rad]$ in the vertical plane, while the phase advance between the sextupoles further away from the injection straight is $0.99 \cdot 2\pi$ $[rad]$ and $0.36 \cdot 2\pi$ $[rad]$ for the horizontal and the vertical plane, respectively. For acquiring turn-by-turn data after a beam excitation, 21 beam position monitors are installed in the IOTA ring, with at least two BPMs per straight section.

In Fig. 4, the baseline optics for the nonlinear integrable optics studies in the IOTA ring is presented, with a working point of $Q_{x,y} = 5.3$.

The sections marked in light grey and light green illustrate the location of the NL-magnet and the octupole string, respectively, with both fulfilling the constraint illustrated in Fig. 1, of equal β-functions in both planes. The phase-advance over each insertion is matched to $\mu_{x,y} = 0.3$. The phase advance between the right hand side of the grey marked section to the left hand side of the same section is matched to an integer phase-advance. The same holds true for the section containing the octupole string, marked in green.

4 Experimental setup and measurements

Various methods exist for the assessment and localisation of nonlinear magnetic fields in an accelerator. For the studies presented in this note, a beam-based approach is chosen, in particular looking into the turn-by-turn motion of a transversally excited particle bunch. The spectral content of transverse beam position evolution after the excitation, recorded around the ring by the 21 Beam Position Monitors (BPM), provides insights into the linear optics and the characterisation of the nonlinear motion via (combined-) resonance driving terms (RDT) [11]. By combining the data from different locations around the ring, the location of strong sources may be inferred.

The turn-by-turn measurements were conducted during 3 non-consecutive shifts, where both the NL-magnet and the octupole channel were turned off to conduct bare lattice measurements.

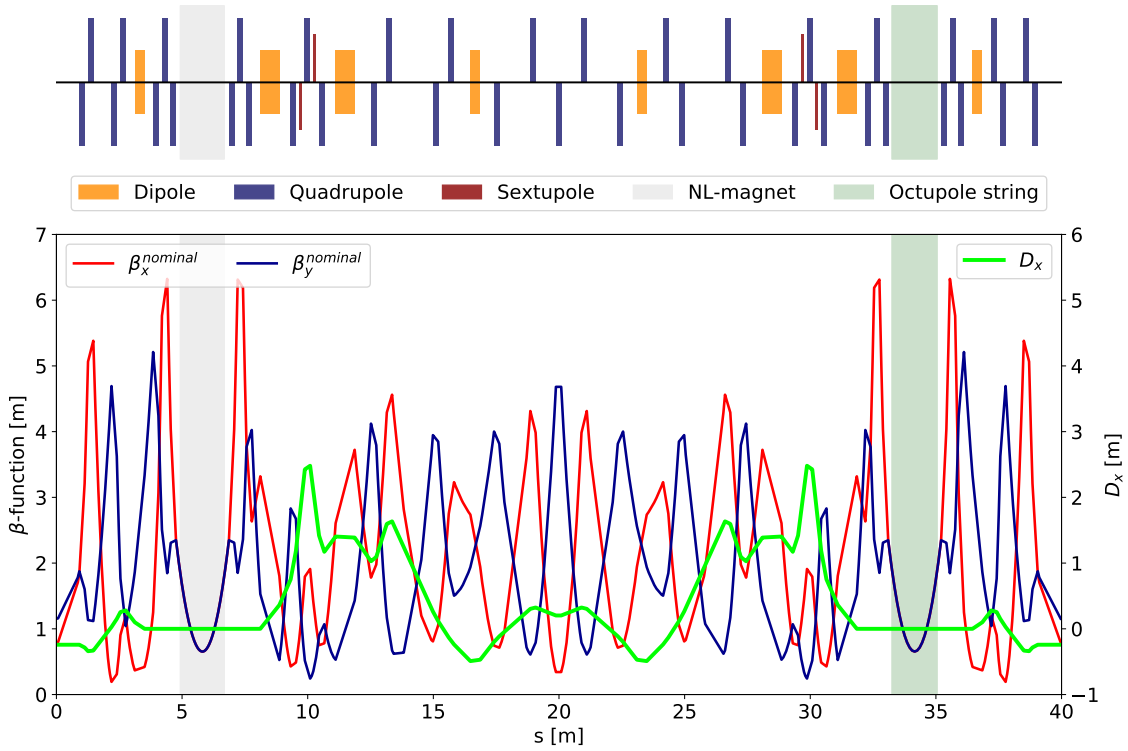

Figure 4: Baseline optics for the nonlinear integrable optics studies, starting from the injection point.

Data taking for the different analysis scenarios was split up over the three shifts as follows:

Shift 1: Date: 02.03.2020, Data available under [12]

- Data captured at a working point of $Q_{x,y} = 5.3$ with excitation in both planes, both on- and off-momentum, using nominal sextupole correction settings
- Data captured at a working point of $Q_x = 5.28/Q_y = 5.31$ with excitation in both planes, both on- and off-momentum, using nominal sextupole correction settings

Shift 2: Date: 04.03.2020, Data available under [13]

- Data captured at a working point of $Q_{x,y} = 5.3$ with excitation in one planes for amplitude detuning measurements, using nominal sextupole correction settings
- Data captured at a working point of $Q_{x,y} = 5.3$ with excitation in one planes for amplitude detuning measurements, with sextupoles turned off
- Data captured at a working point of $Q_x = 5.28/Q_y = 5.31$ with excitation in one planes for amplitude detuning measurements, using nominal sextupole correction settings
- Data captured at a working point of $Q_{x,y} = 5.3$ with excitation in both planes for RDT measurements, with sextupoles turned off
- Data captured at a working point of $Q_x = 5.28/Q_y = 5.31$ with excitation in both planes for RDT measurements, with sextupoles turned off

Shift 3: Date: 07.03.2020, Data available under [14]

- Data captured at a working point of $Q_x = 5.28/Q_y = 5.31$ with excitation in both planes for RDT measurements, with sextupoles in section CR turned off
- Data captured at a working point of $Q_x = 5.32/Q_y = 5.29$ with excitation in both

both the sextupoles closer to the injection point and those further away, and chromaticity was corrected to $Q'_x = Q'_y = 0$. Notably, the natural chromaticity of the accelerator does not match the model values, the working assumption being an additional sextupole component from the 60° dipoles. Both measures aim to reduce decoherence to provide a sufficient number of turns. In Fig. 5, a typical example of turn-by-turn motion recorded by one BPM is illustrated. Here, the number of usable turns before the signal is damped down is about

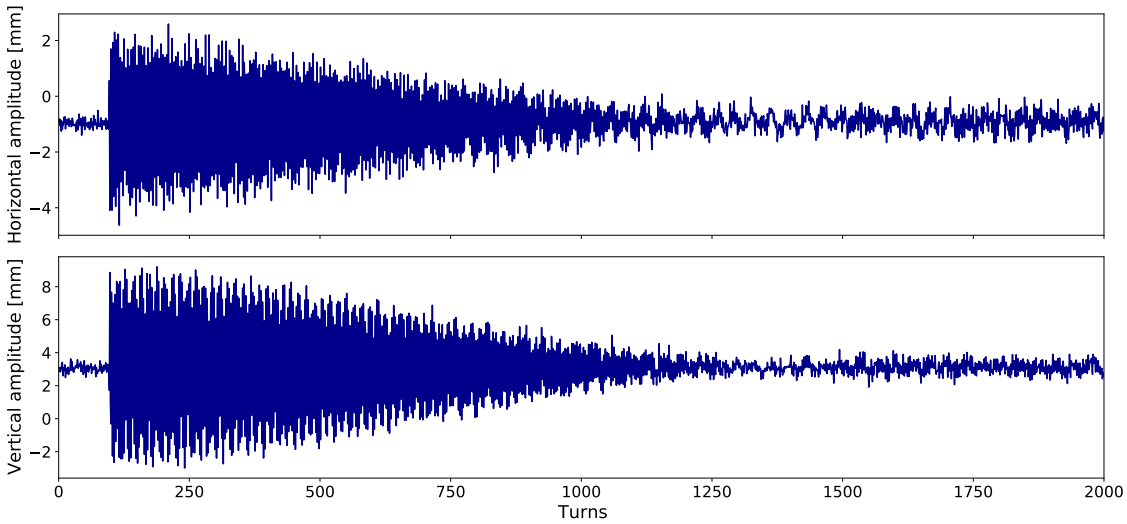

Figure 5: Turn-by-turn motion after one excitation recorded by the IBPMB2L.

900 turns. As the synchrotron radiation damping time is relatively long ($> 10^7$ turns) [7], the damping mainly stems from the decoherence, and here in particular from decoherence due to amplitude detuning, as chromaticity is matched to 0 [15].

Data was taken using either the baseline optics with a working point of $Q_x = Q_y = 5.3$ or with working points with larger tune separation, namely using $Q_x = 5.28/Q_y = 5.31$ and $Q_x = 5.32/Q_y = 5.29$. The tunes were changed using the knobs as presented in Tab. 1.

The working point change is achieved by mostly adjusting the β-function in the injection straight, as is displayed in Fig. 6, with the maximum change of the β-function below 10%.

Working points other than the nominal one were chosen for measurements of (C-)RDTs as to distinguish between certain lines more easily. An example is displayed in Fig. 7.

Here, for the case of the nominal working point, for example, the sextupole lines $H(-2, 0)$ and $H(0, -2)$ overlap and the octupole line $H(-1, 2)$ lies in the shadow of the main tune line, making the reconstruction rather difficult or next to impossible, which is not the case for the separated working point. However, the change in working point also entails a change of the amplitude of the (C-)RDTs and subsequently the amplitude of the spectral lines is changed between these two cases. Thus, the derived resonance strength is not representative for the case of the nominal optics. Still, the measurements allow to benchmark the nonlinear model and infer location and strength of nonlinear magnetic fields.

Magnet	$\Delta K/\Delta Q_x$ $[10^{-3}/m^2]$	$\Delta K/\Delta Q_y$ $[10^{-3}/m^2]$
QA1R	−2.56	7.62
QA2R	16.84	−2.54
QA3R	4.36	11.61
QA4R	−23.34	−3.40
QB1R	−0.17	−32.40
QB2R	11.83	8.80
QB3R	−0.64	−1.30
QB4R	−2.87	−6.11
QB5R	4.25	9.01
QB6R	−6.11	−12.95

Table 1: Knobs used to change horizontal and vertical tune. Note that due to symmetric optics, the same change is applied in the quadrupoles on the left hand side.

The presented measurements were analysed using the `python 3.7` based OMC3 software suite [16], and crosschecked with its predecessor [17], implemented in `python 2.7`. The turn-by-turn data was cleaned before spectral composition, using a variety of cut-based methods, e.g. removing BPMs where the oscillation exceeds a given threshold, and removing noise by performing a singular value decomposition, retaining only a number of modes with the largest singular values [18]. The number of modes was chosen based on the analysis, with the (C-)RDT analysis using a significantly higher number compared to the linear optics one to be able to show local phenomena [19].

4.1 Linear Optics

As demonstrated in [20], good control of the linear optics is among the key issues, critical to achieving a large tune spread while keeping particle losses minimal. Similarly so, good knowledge of the linear optics is also critical as a precursor to evaluating nonlinear observables. For the commissioning of the linear optics, a LOCO algorithm is regularly used [21], with good results achieved in the previous run [22]. Complementary to the LOCO based approach, as a first step before analysing higher order modes in the spectral components of the motion, the linear optics is inferred from the captured turn-by-turn data. Two methods were used to infer the linear optics, one based on the measured phase advance between BPMs and one based on the amplitude of the oscillation.

For the phase advanced based approach, the N-BPM method [23, 24] is employed, using combinations of 7 surrounding BPMs to the one probed. This approach uses measured and model phase advances between BPMs together with the model β-functions at the BPMs to determine the β-function at a certain BPM. In Fig. 8, the difference between model and measured phases between consecutive BPMs is presented.

The phase advance in the nonlinear channel on the left hand side of the plot is well controlled, approaching the desired 10^{-3} level. In the octupole channel on the right side of the plot on the other hand, a larger phase difference is noted. It has to be noted that this measurements

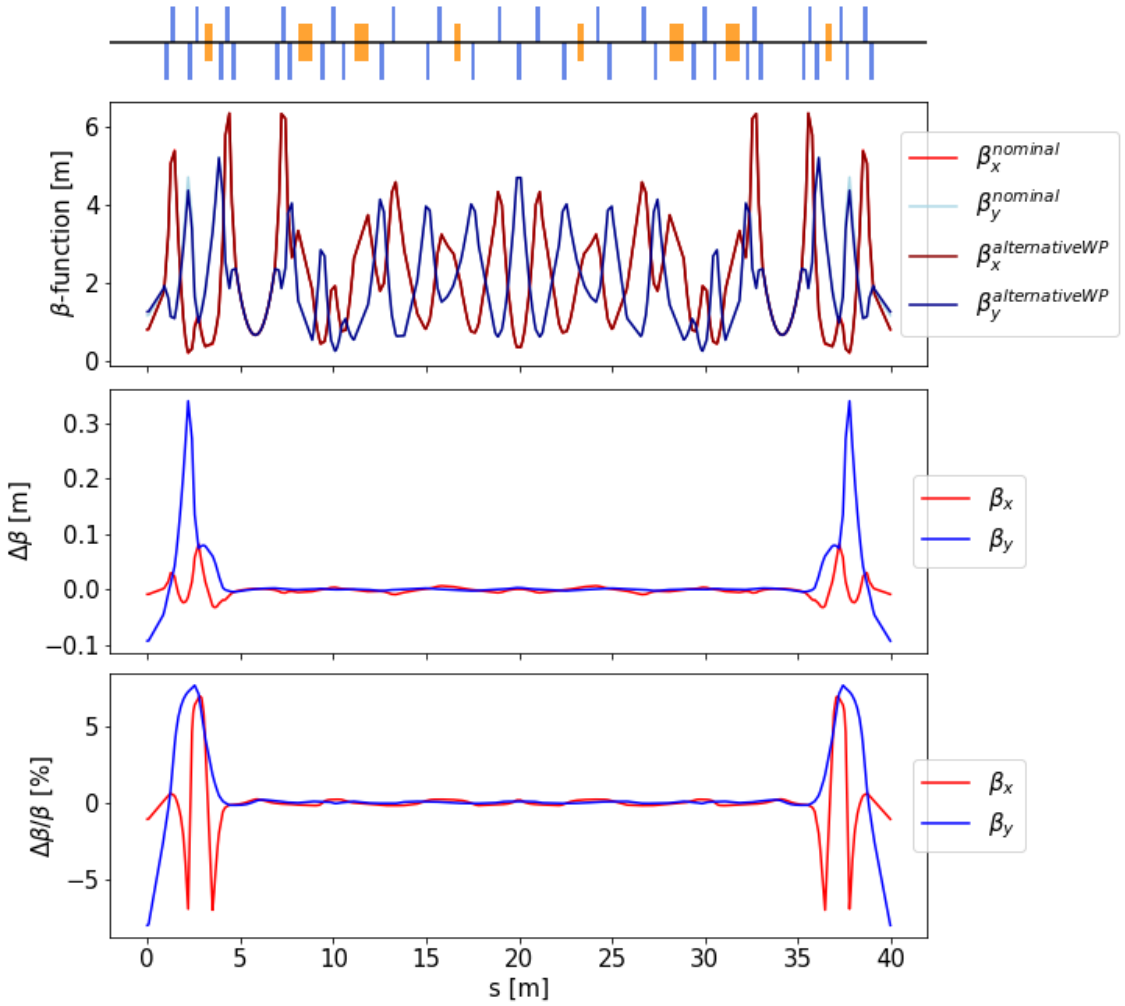

Figure 6: Change of the optics when moving from the nominal optics to a working point of $Q_x = 5.28$, $Q_y = 5.31$.

were conducted with a non-nominal optics at a working point of $Q_x = 5.28$, $Q_y = 5.31$ and without any prior corrections applied, as such not being able to accurately reflect the levels reached in operation.

Using the the measured phase difference as input and the aforementioned N-BPM algorithm, the β-functions were determined and are displayed in Fig. 9.

Although no optics correction were performed after the application of the tune knob, the presented results show a peak β-beating below 12 % around the IOTA ring, above the target accuracy for the experiments with the NL-magnet, but well with the parameters for experiments with the octupole channel [22]. Notably, the results in the horizontal plane are worse, likely due to reduced number of usable turns in this plane and thus reduced phase accuracy.

The other approach for determining the optics functions around the ring, using the oscillation amplitude of the betatron motion, dubbed β from amplitude [25], critically depends on the

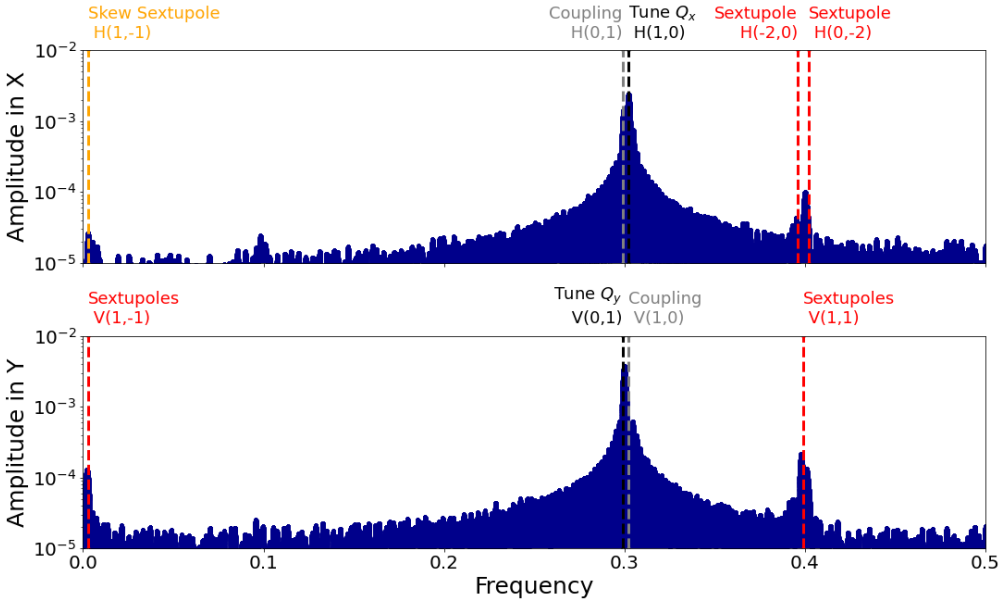

(a) Working point $Q_x = Q_y = 5.30$

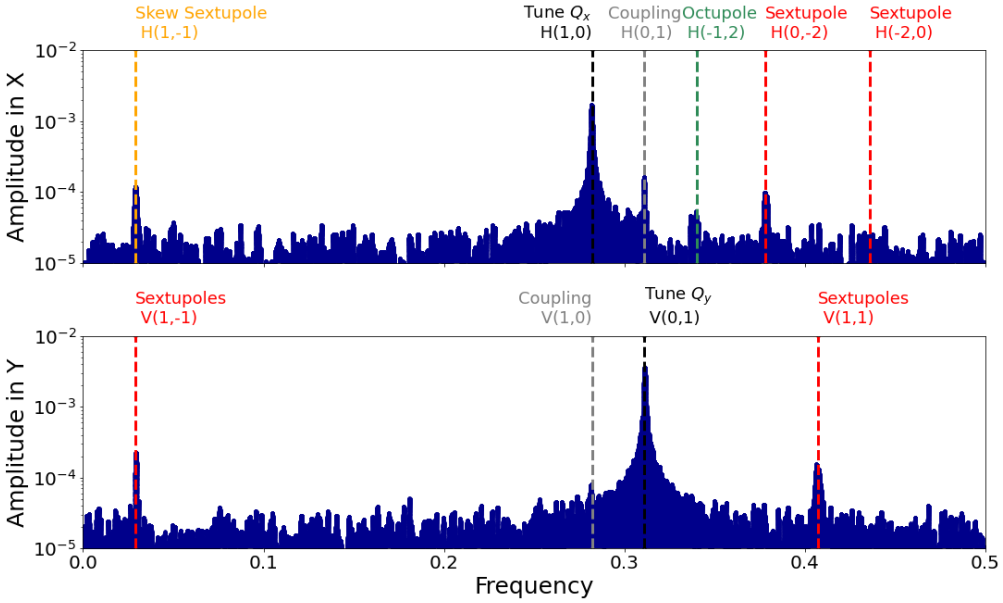

(b) Working point $Q_x = 5.28$, $Q_y = 5.31$

Figure 7: Comparison between spectra for the nominal working point ($Q_x = Q_y = 5.30$) and a working point with a larger tune separation.

calibration of the individual BPMs and on the accuracy of the kick action determination. The kick action is determined using

$$2J_{x,y} = \frac{\sum_{BPMs}(0.5A_{x,y})^2/C_{x,y}^2\beta_{x,y}}{N_{BPMs}} \ , \tag{10}$$

where $A_{x,y}$ is the peak-to-peak amplitude of the oscillation at the given BPM, $\beta_{x,y}$ the beta-function from the model at the respective BPM, N_{BPMs} the number of the BPMs, and

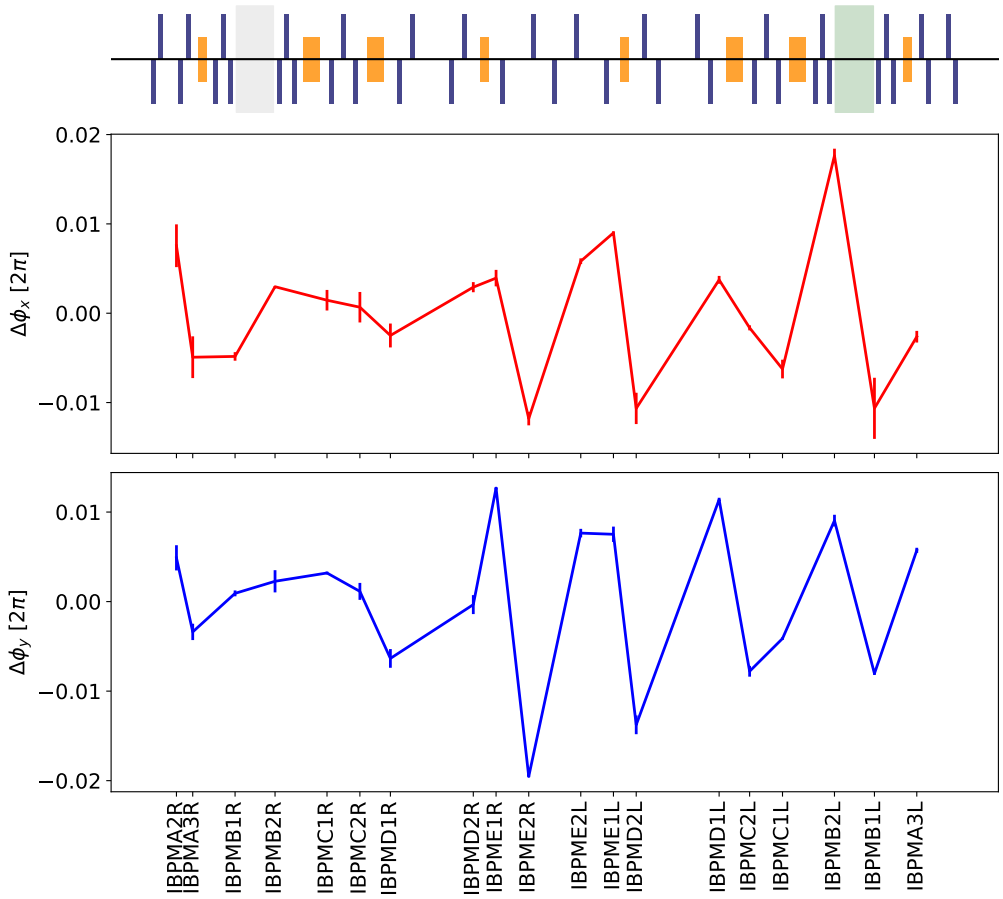

Figure 8: Difference between measured and model phase advance. The phase difference at given BPM represents the difference with respect to the next BPM.

$C_{x,y}$ represents the, a priori unknown, calibration factor of the given BPM. The underlying assumptions for the use of this formula are that the effect of linear coupling on the action, as well as that the phase space distortion from higher order resonances are negligible, and that by averaging over all BPMs, first order effects from optics errors are canceled and the remaining higher order having no significant impact. The β-function at a given BPM is then inferred via

$$\beta_{x,y} = \frac{A_{x,y}^2}{C_{x,y}^2 2J_{x,y}} \ . \tag{11}$$

The calibration factor may be inferred later by comparing to trusted optics measurements from LOCO. However, given the exploratory nature of the presented measurements, the determination of the calibration factors and validation was deemed outside of the scope of this work. In Fig. 10, the results using the β from amplitude method are displayed.

For the presented measurements, the BPM `IMBPMA1C` has been excluded, as across all measurements it has shown a significantly lower β-function, which is attributed to this BPM featuring an alternate design with a wider aperture [7] and its position readout not adapted to the different geometry compared to the other BPMs. Compared to the previously presented β from phase result, the β from amplitude measurements show a higher β-beating, with a

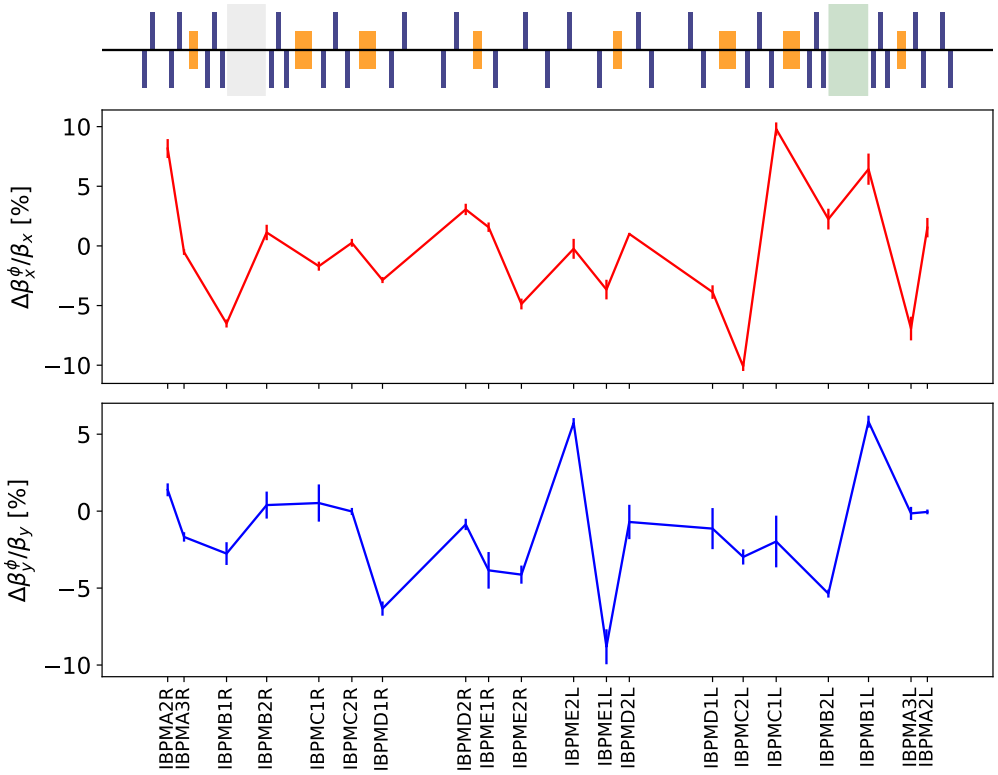

Figure 9: Measured β-beating using the analytical N-BPM method.

peak deviation of about 15 % compared to the 12 % found before. As mentioned before, this could partly be attributed to the calibration issues in BPMs. Additionally, the action calculation may be improved by using measured β-function from LOCO measurements. However, in both measurements a significant beating is found close to the octupole string and in the injection straight, where also the optics was changed to achieve the change in tunes. Similar results have also been obtained for data sets from later measurements shift using the same working point.

Notably, in both analyses, multiple data sets show erratic behaviour, not present in the kick immediately before and after this data set. No immediate explanation for these transients has been been found and data sets with large deviations in the optics have been dropped.

While not definite results and with potential for further improvements, studies and cross-checks with LOCO, the results indicate that, as expected, the linear optics is sufficiently well controlled for the following studies and no special precaution were deemed necessary for the following analysis. However, the target β-beating below 1% is not yet observed using turn-by-turn based methods for measuring the linear optics.

4.2 Amplitude detuning

The nonlinear integrable optics concept is based on generating a tune spread via detuning with amplitude, which allows mitigation of coherent instabilities. As such, to determine the amplitude detuning from the nonlinear inserts, it is also of particular interest to determine

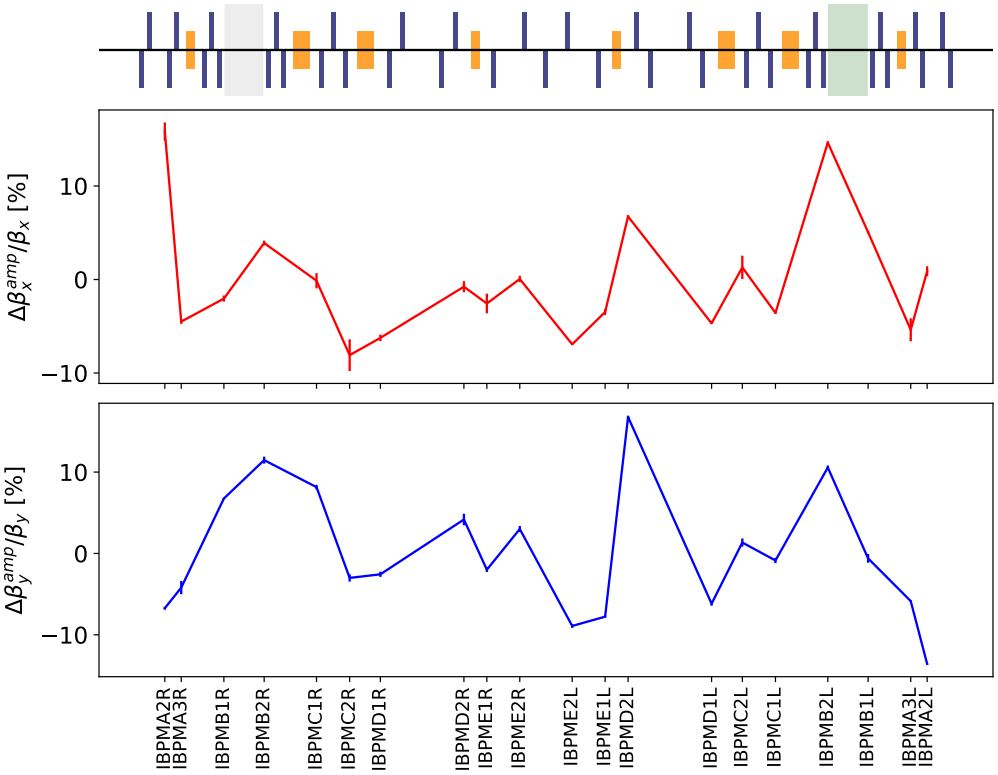

Figure 10: Measured β-beating using the β from amplitude method.

the detuning of the bare accelerator with both nonlinear inserts turned off. Given that detuning from the nonlinear inserts and from other sources of the accelerator is to first order independent, the impact of the lattice sources could then be used together with the measured detuning with the nonlinear inserts to compare with theoretical estimates. In Tab. 2, the expected amplitude detuning from the model is shown for the case where the sextupoles are used in their nominal configuration and for the case of a sextupole component in all 60° dipoles of $k_3L = 4.55$ m^{-2}, compared to $k_3L = -40$ m^{-2} and $k_3L = 55$ m^{-2} of the chromaticity sextupole when powered in their nominal correction scheme. The sextupole component in the dipoles has been implemented such that it matches with the measured chromaticity in the IOTA ring when the chromaticity sextupoles are turned off.

Sources	**chromaticity sextupoles**	**chromaticity sextupoles + dipole b_3 errors**	**NL-magnet with t=0.29**
$dQ_x/d2J_x$	150	19	575
$dQ_x/d2J_y$	294	209	-2207
$dQ_y/d2J_y$	100	100	2126

Table 2: Amplitude detuning in the IOTA ring for different sources.

Additionally, for comparison, the amplitude detuning for an ideal lattice without sextupoles and the nonlinear insert powered to $t = 0.29$ is presented here too. Notably, the effect of the b_3 errors is most pronounced in the direct horizontal detuning, showing a decrease of almost

a factor 10 from the unperturbed case. Similarly so, based on the model, the powering of the chromaticity sextupole generates up to 20% of the amplitude detuning generated by the NL-magnet, in particular for the direct term in the horizontal plane, and to a lesser extent in the cross-plane detuning. In simulations, the amplitude detuning generated by the chromaticity sextupoles decreases the horizontal direct term by 25% when changing to a working point with split tunes such as $Q_x = 5.28$, $Q_y = 5.31$, with the other terms changing by less than 5%.

For the measurements of the detuning in the bare lattice, the beam was excited in both planes. The strength in one plane is stepwise increased while the kick strength in the opposite plane remains the same throughout the measurement. This was done as to provide enough excitation in the non-ramped plane to determine the tune in this plane, such that the cross-plane detuning may also be determined. Given the small and constant excitation strength in the cross-plane, any change of the tune here is then fully attributed to the excitation of the plane where the excitation strength is ramped up. In turn, a potential contribution due to linear coupling is hereby neglected in this approach.

As noted in the previous section, the kick action $2J$ is then inferred for plane where the kick strength has been gradually ramped up. Again, in order not to distort the action calculation, for the analysed data sets, the turn-by-turn data of `IBPMA1C` has been dropped.

Measurements were conducted using an optics with a working point of $Q_x = 5.28$, $Q_y = 5.31$. Sextupoles were set such that the chromaticity is matched to 0. The measured amplitude detuning is presented in Fig. 11.

It has to be noted that only a smaller number of kicks was available at this working point, in particular for the horizontal kicks. Furthermore, no online continuous tune measurements system is present, such that data could not be corrected for any possible tune drift. Notably, the measured detuning does not agree with the previously presented expected detuning from the two models. The summary of the measurement and a comparison to the model values for the working point $Q_x = 5.28$, $Q_y = 5.31$ is given in Tab. 3.

Sources	**chromaticity sextupoles**	**chromaticity sextupoles + dipole b_3 errors**	**Measurement**
$dQ_x/d2J_x$	112	10	412 ± 75
$dQ_x/d2J_y$	287	202	-241 ± 38
$dQ_y/d2J_x$	287	202	-310 ± 8
$dQ_y/d2J_y$	95	96	303 ± 9

Table 3: Measured amplitude detuning in the IOTA ring together with a comparison to the detuning expected from the model.

Although measurements with horizontal kicks are sparse, the horizontal detuning is about a factor 4 larger than what is expected and is about the size as the direct horizontal detuning from the NL-magnet at $t = 0.29$. Furthermore, the cross term detuning in both cases shows an opposite sign of what is expected from the model and approximately the same order of magnitude, hinting at possible extra sources of detuning in the bare lattice. While

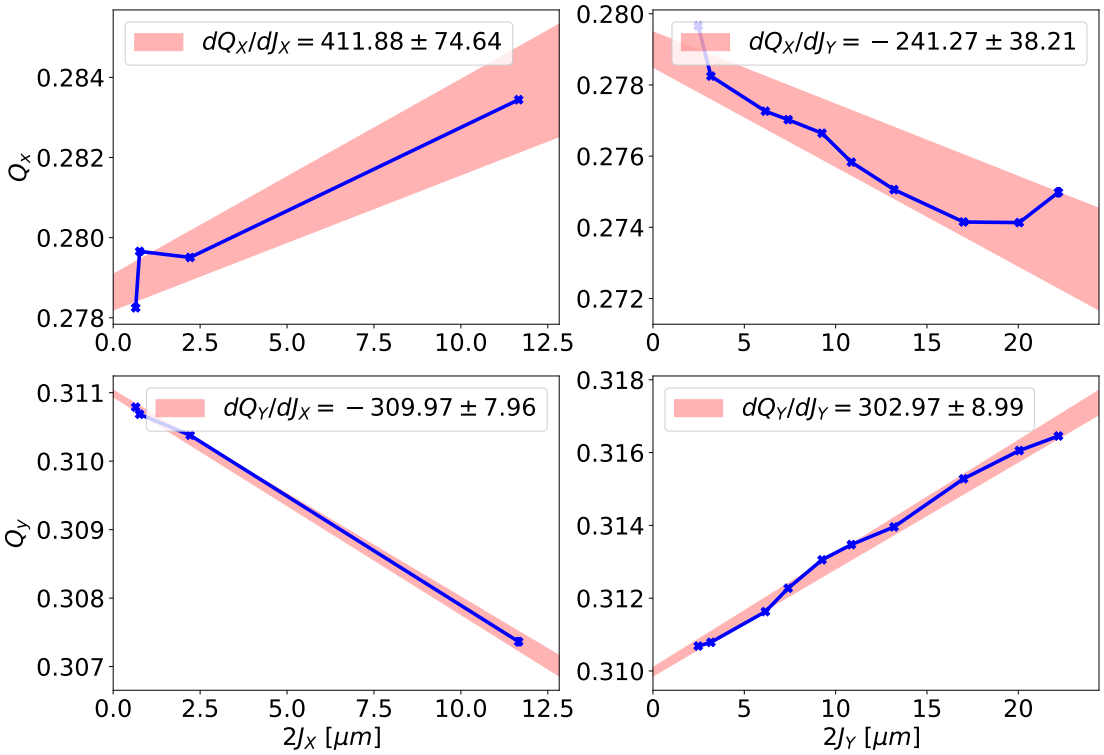

Figure 11: Measured amplitude detuning using an optics with a working point of $Q_x = 5.28$, $Q_y = 5.31$. A linear fit over the presented data is displayed in red, together with the amplitude detuning obtained from the fit.

inconsistent with behaviour expected if sextupoles are the main contributors to the detuning, the measured detuning is more consistent with an octupole as main source. From these measurements however, the number and strength of octupole sources cannot be concluded. One potential candidate could be hysteresis effects in the octupole string. It should be noted that before these measurements were conducted, the center octupole was degaussed and another one was disconnected due to issues with the powering.

Further amplitude detuning analysis was performed for data obtained from a later shift, using an optics with the same working point of $Q_x = 5.28$, $Q_y = 5.31$. As this data was primarily taken for (C-)RDT analysis, kick amplitudes were not optimized for amplitude detuning analysis and the kick strength in the non-ramped plane was unnecessarily high. Due to this, a non negligible contribution from the kick action of the off plane may arise, potentially spoiling the measurement accuracy. Additionally, a non-nominal sextupole configuration was used, with only two sextupole from the same straight section used to correct for chromaticity. In Fig. 12, the results of the amplitude detuning analysis are shown, with a comparison to the expected model detuning presented in Tab. 4.

Compared to the previous analysis, a better agreement with the model values is observed in this case. In particular, no opposite sign in the cross detuning is found, thus it is assumed that sextupole are the main contributor to the detuning in this scenario and no strong spurious octupole source appears to be present during that shift. These results also add to

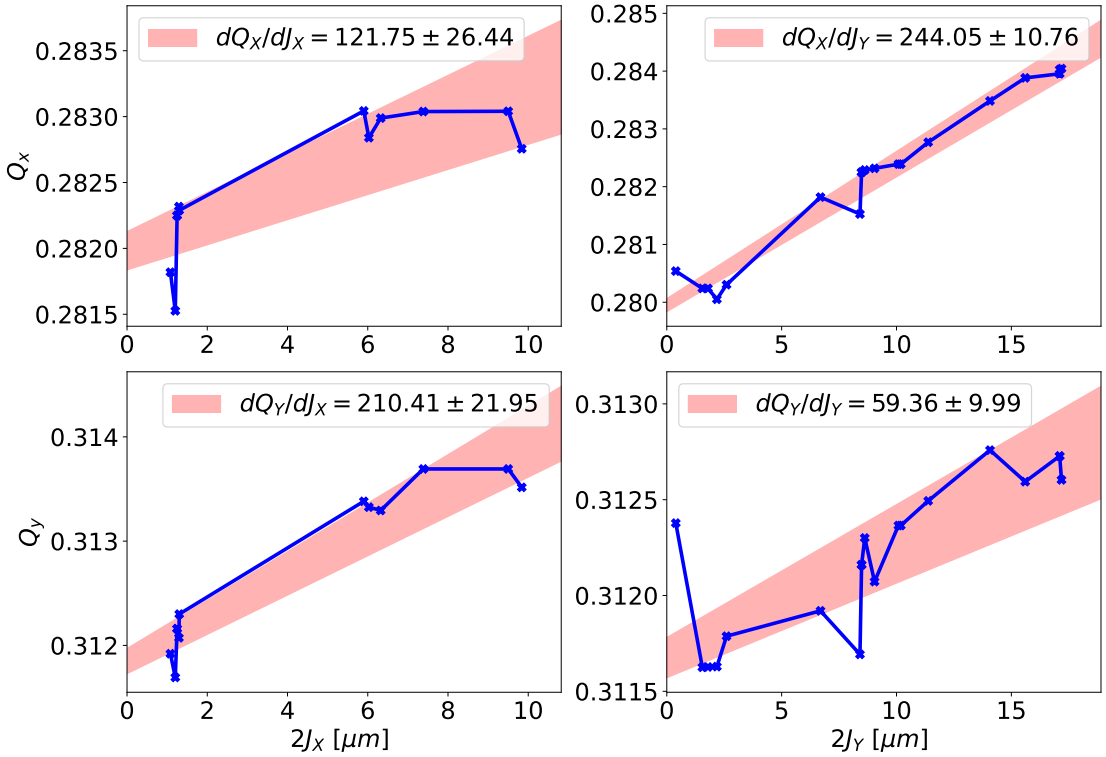

Figure 12: Measured amplitude detuning using an optics with a working point of $Q_x = 5.28$, $Q_y = 5.31$ and using only sextupoles from the left hand straight section for chromaticity correction. A linear fit over the presented data is displayed in red, together with the amplitude detuning obtained from the fit.

the previous suspicion that the previously observed strong octupole contribution might be linked to the intervention performed before the measurements. While this measurements only provide a snapshot over a short time span, based on these results, no persistent strong spurious octupole source appears present and, bar any hardware issues, amplitude detuning seems mostly by the chromaticity sextupoles.

4.3 (Combined-) Resonance Driving terms

As motivated in Sec. 2, good knowledge of the nonlinear elements outside of the nonlinear channel is of great importance for assessing the performance of NL-magnet. Using a nonlinear model, validated by the measurements, more realistic simulation can be performed to estimate the performance. In the following, also potential correction strategies may be tried in simulation and, provided a viable solution is found, then be implemented in the accelerator.

For assessing the validity of the IOTA model, as a first measure the so-called combined resonance driving terms [11] were assessed. In this method, the spectral line amplitude for certain resonances is used to infer a linear combination of two resonance driving terms. As such, the strength of individual RDTs cannot be inferred from the measurements. Furthermore,

Sources	**chromaticity sextupoles**	**chromaticity sextupoles + dipole b_3 errors**	**Measurement**
$dQ_x/d2J_x$	150	45	121 ± 26
$dQ_x/d2J_y$	302	209	244 ± 11
$dQ_y/d2J_x$	302	209	210 ± 22
$dQ_y/d2J_y$	225	199	59 ± 10

Table 4: Measured amplitude detuning at a working point of $Q_x = 5.28$, $Q_y = 5.31$ and using only sextupoles from the left hand straight section for chromaticity correction, together with a comparison to the detuning expected from the model.

this method relies on the use of dual plane BPMs, which is the case in IOTA.

The C-RDT are measured by determining the kick action and amplitude of a specific spectral line at each BPM. The C-RDT is then obtained by performing a linear fit for various measurements with different kick action and line amplitudes using the relations for the individual C-RDT as presented in [11] and as is illustrated in Fig. 13. It has to be noted that for the analysis here, spectral lines were normalised with the main line of the respective plane to account for first order calibration errors. As such, during the fitting process, an additional contribution from the kick action has to be taken into account.

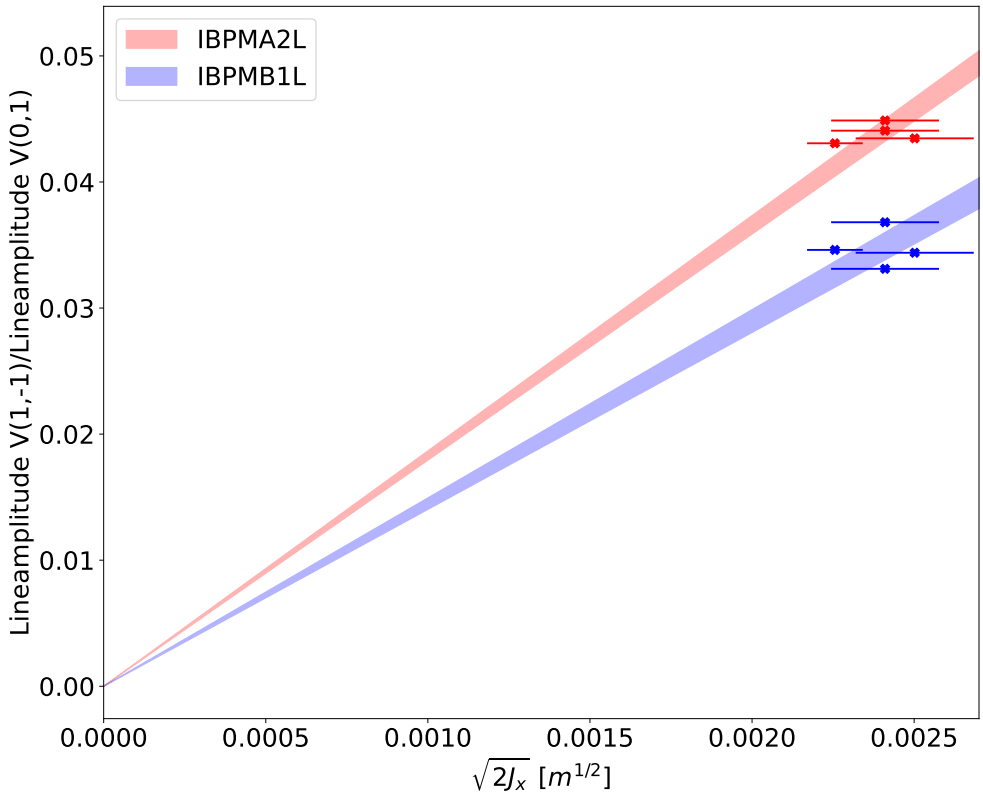

Figure 13: Amplitude of the V(1,-1) line for different kicks at 2 BPMs. Overlayed a linear fit to obtain the CRDT at the given BPMs.

Note that in the following, a different notation compared to the original paper [11] will be adapted, namely, C-RDT will be addressed by their corresponding line. As example, the C-RDT F_{NS3} will be addressed by $H(-2, 0)$, corresponding to the line $-2Q_x$ in the horizontal spectrum.

First C-RDT measurements were performed at a working point of $Q_x = 5.28$, $Q_y = 5.31$ and using a nominal sextupole configuration. C-RDTs were only investigated for lines which were clearly above the noise level in all BPMs, which limit the analysis to coupling, sextupoles, skew sextupoles, and octupole C-RDTs. In Fig. 14, the measured coupling C-RDTs are presented. A notable excursion is observed in the injection straight for the C-RDT $H(0, 1)$. Following the derivations presented in [26, 27], this indicates a strong influence of the horizontal motion on the vertical one here. This may be of concern as both the horizontal and vertical kicker are located here.

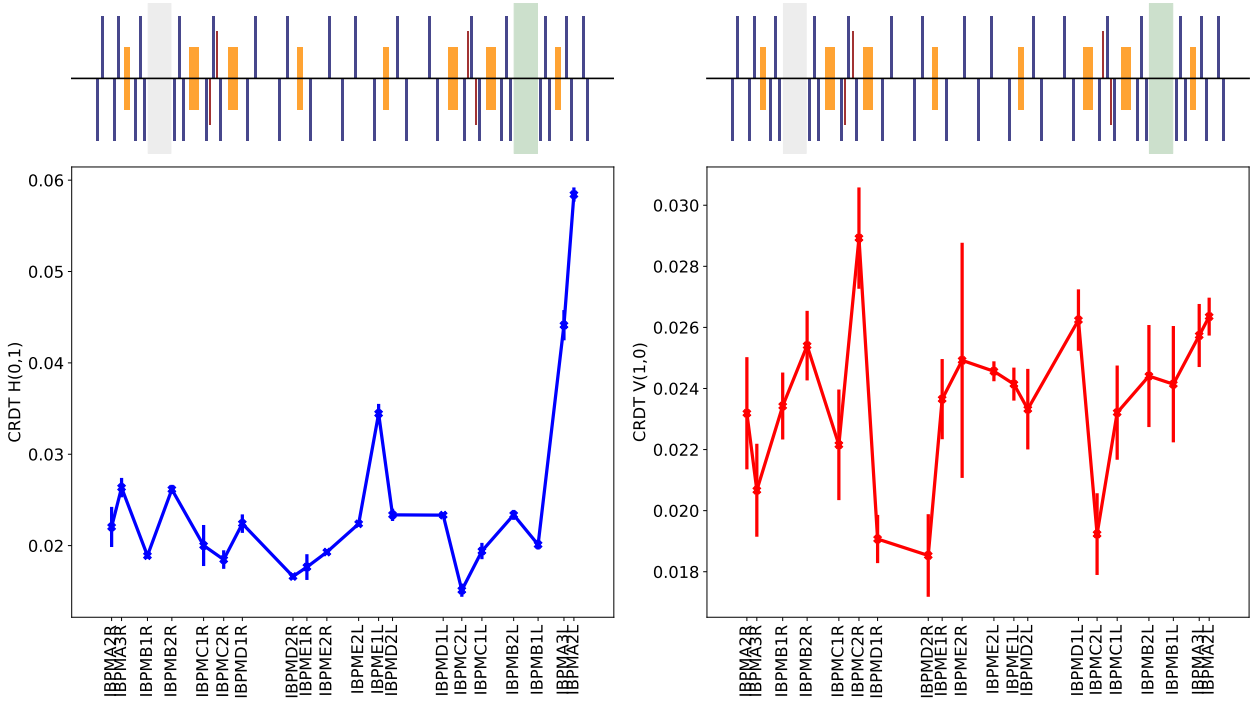

Figure 14: Measured coupling C-RDTs at a working point of $Q_x = 5.28$, $Q_y = 5.31$ and using a nominal sextupole configuration.

In Fig. 15, the amplitude of the sextupole C-RDTs are presented.

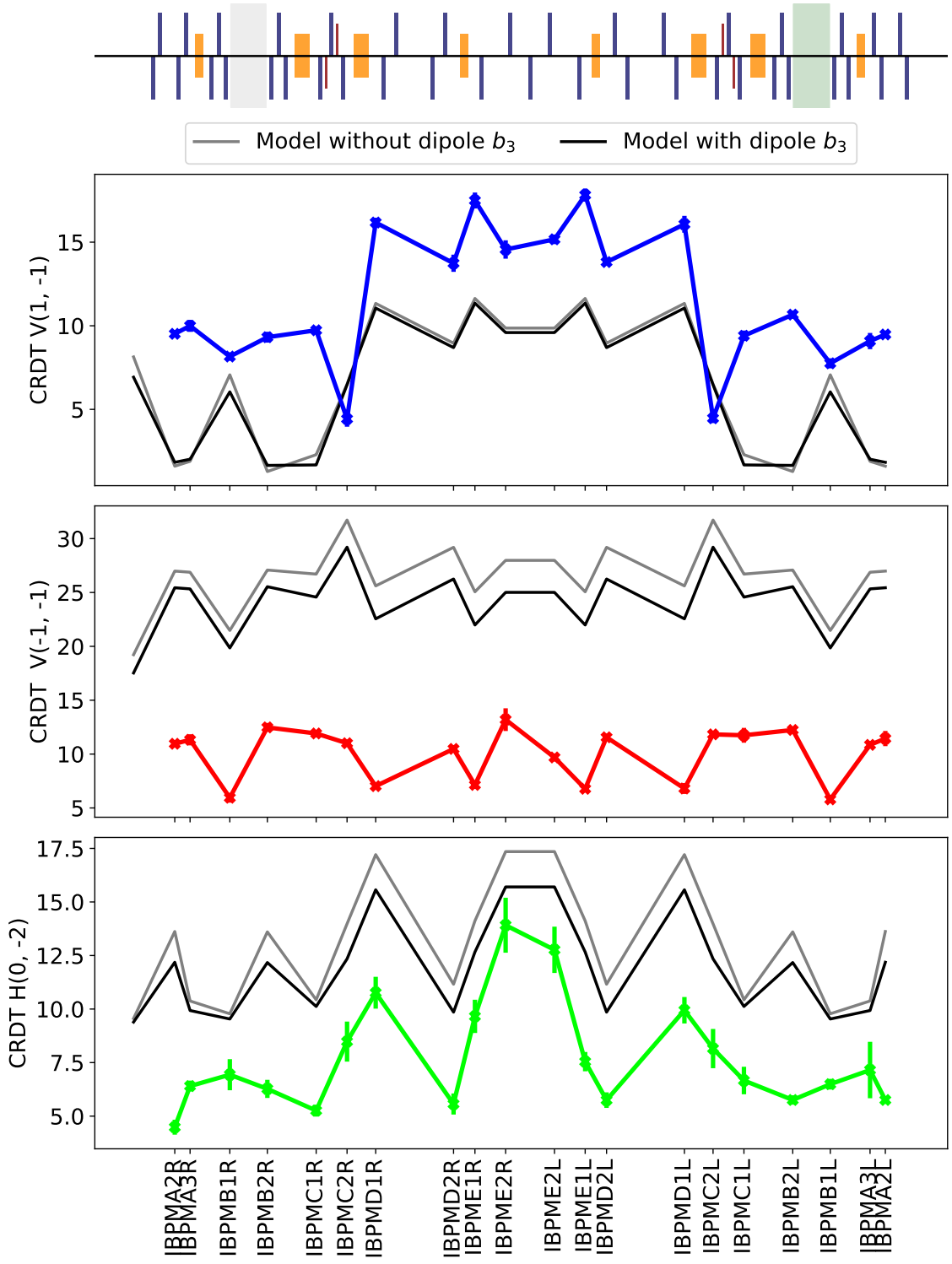

Figure 15: Measured sextupole C-RDTs at a working point of $Q_x = 5.28$, $Q_y = 5.31$ and using a nominal sextupole configuration, together with a comparison to the expected model values.

Here, the C-RDT corresponding to the line $H(-2, 0)$ is not presented, as the line was not observed in the spectra. Additionally, the model sextupole C-RDTs, evaluated using MAD-X PTC, are included for the case of the nominal chromaticity correction and when including a sextupole component in the 60° dipoles. Notably, a discrepancy between the model amplitude and measured amplitude is observed in all cases. However, it has to be noted that the different decoherence factor for the spectral lines [5] have not been applied yet to the data. The difficulty in determining those lies in that here both planes need to be taken into account, for which case no analytical solution has been found. As such, decoherence factors need to be obtained via numerical integration, which for the time being has not yet been performed. However, a good qualitative agreement in the longitudinal evolution of the C-RDTs is observed. Given the small expected change from a potential sextupole component in the dipoles and the discrepancy in the amplitude, no conclusion on the presence of such errors can be made at the moment.

One skew sextupole line was consistently observed in all BPMs and for different kicks and the corresponding C-RDT is presented in Fig. 16.

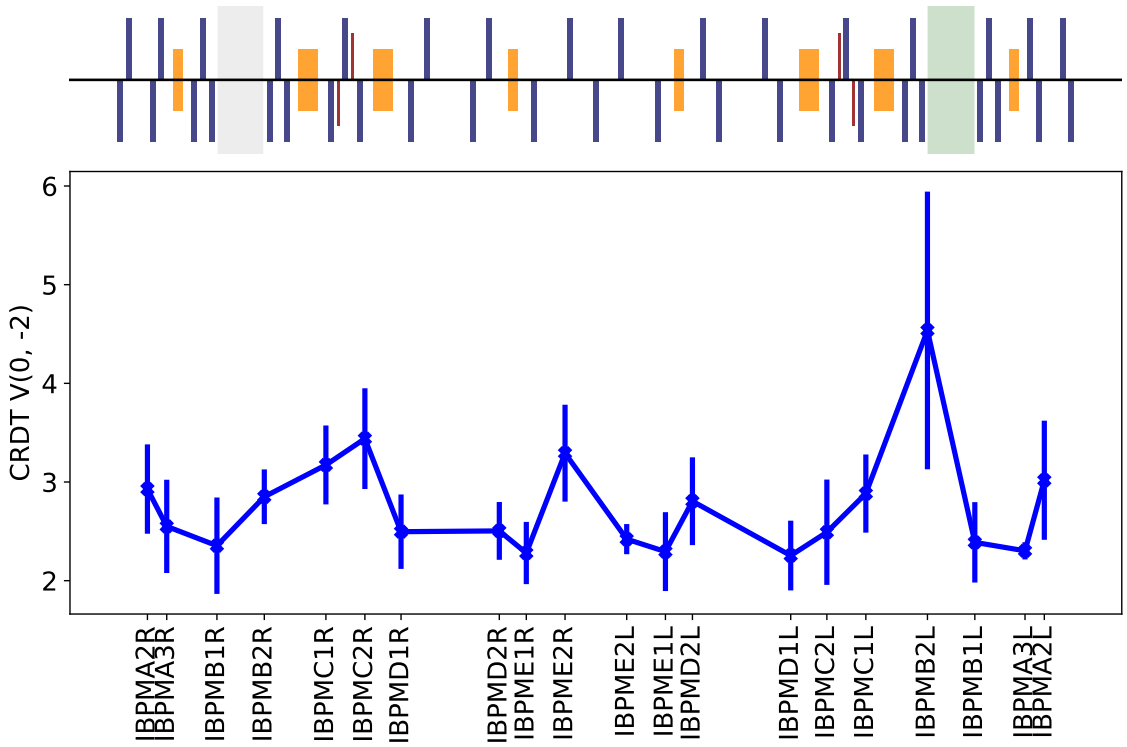

Figure 16: Measured skew sextupole C-RDT at a working point of $Q_x = 5.28$, $Q_y = 5.31$ and using a nominal sextupole configuration.

Notably, given that by design no skew sextupole sources are present in the IOTA-ring, the presence of such line can be explained either by sextupole tilts, by an interplay between linear coupling and the regular sextupole sources, or any combination of those two effects. Similar to the sextupole lines, no decoherence factors were applied so far and thus the data cannot be used yet to determine the origin.

Lastly, in Fig. 17, the C-RDT corresponding to the line $H(-1, 2)$, observed in all BPMs is presented.

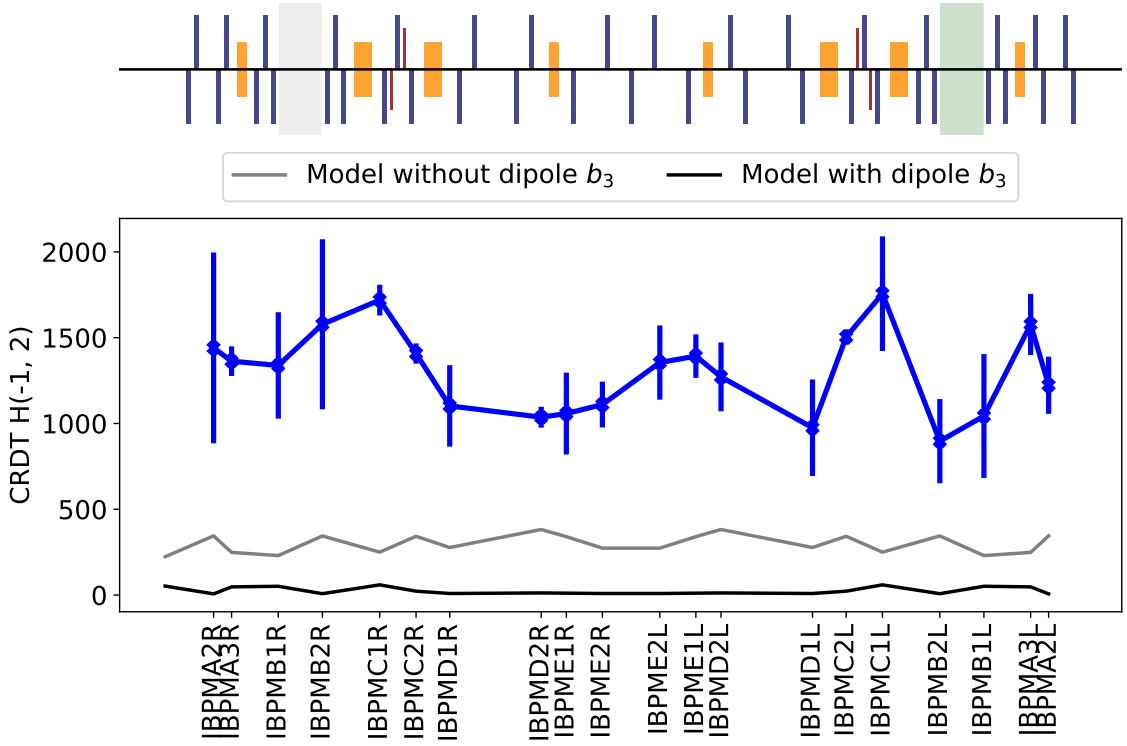

Figure 17: Measured octupole C-RDT at a working point of $Q_x = 5.28$, $Q_y = 5.31$ and using a nominal sextupole configuration, together with a comparison to the expected model values.

As octupole lines may also arise from, amongst others, a second order contribution from normal sextupoles, model values have been included here. Again, due to the lack of the decoherence correction, no comparison on the amplitude between model and measurement can be made. However, a difference in the evolution of the C-RDT amplitude is observed, unlike in the previous case for the sextupoles. Further investigation may thus investigate if a spurious octupole source may explain this difference. Notably, this data was taken during a different shift than the amplitude detuning data, as such hinting at a potential consistent octupole source.

In a further shift, studies were performed using a different sextupole powering scheme to potentially better identify any sextupole component in the 60° dipoles. In particular, the sextupoles in the straight section on the right hand side of IOTA-ring, as illustrated in Fig. 3, were turned off and the chromaticity in the ring was corrected using the remaining two sextupoles. Measurements were conducted at a working point of $Q_x = 5.28$, $Q_y = 5.31$, to compare to the measurements conducted in a previous shift, and at working point of $Q_x = 5.32$, $Q_y = 5.29$ and $Q_x = 5.325$, $Q_y = 5.29$. These different working points were chosen due to their proximity to $3Q_x$ resonance and thus increased C-RDTs linked to this resonance.

In Fig. 18-21, C-RDTs for coupling, sextupole, skew sextupole, and octupole sources are presented.

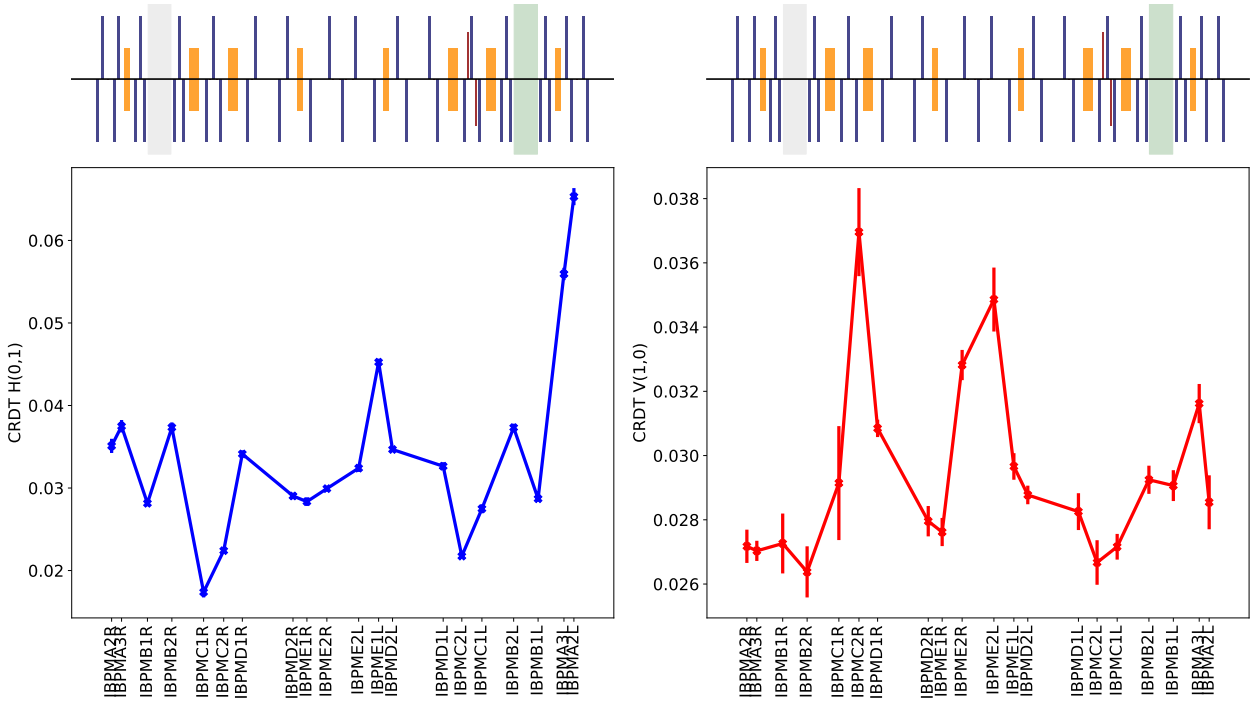

Figure 18: Measured coupling C-RDTs at a working point of $Q_x = 5.28$, $Q_y = 5.31$ and using only sextupoles in the left hand straight section for chromaticity correction.

For the coupling C-RDT $H(0, 1)$, a similar excursion in the injection straight is observed as in the previous dataset, although gathered on different days and shifts. Similar so, a bump in the C-RDT $V(1, 0)$ is observed around `IBPMC2R`.

For the sextupole C-RDTs, similar conclusions as for the previous results hold. While again a good quantitative agreement in the evolution is observed, for a comparison between the model values and the measurements, the difference due to decoherence factors needs to be taken into account. The C-RDT corresponding to the skew sextupole line $V(0, -2)$ does show some consistent behaviour between the two shifts, bar the excursion observed at `IBPMB2L` for the nominal sextupole configuration. Given the similar behaviour of the coupling C-RDTs between the two shifts, no further conclusion on the origin can be made. For the octupole

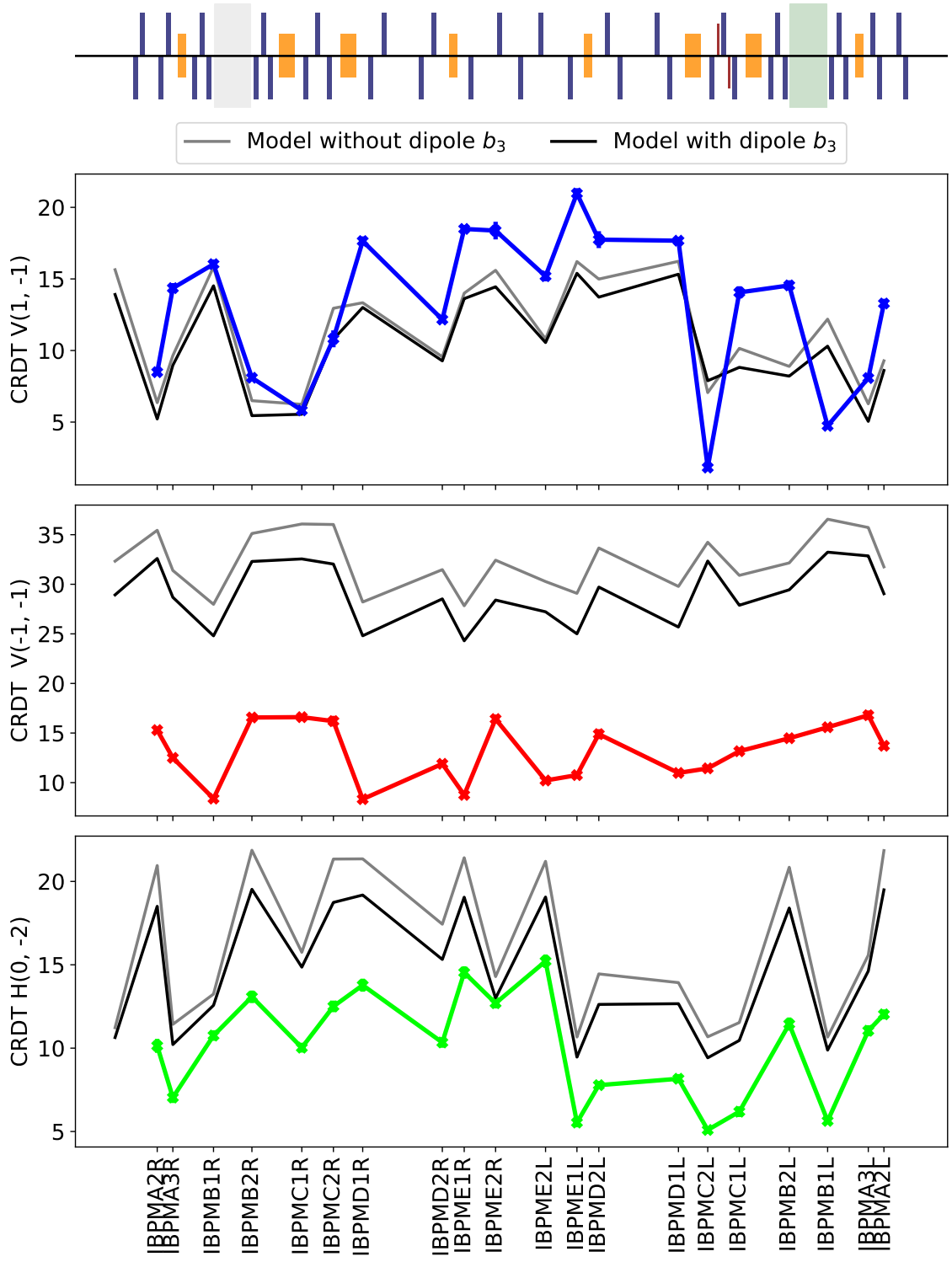

Figure 19: Measured sextupole C-RDTs at a working point of $Q_x = 5.28$, $Q_y = 5.31$ and using only sextupoles in the left hand straight section for chromaticity correction, together with a comparison to the expected model values.

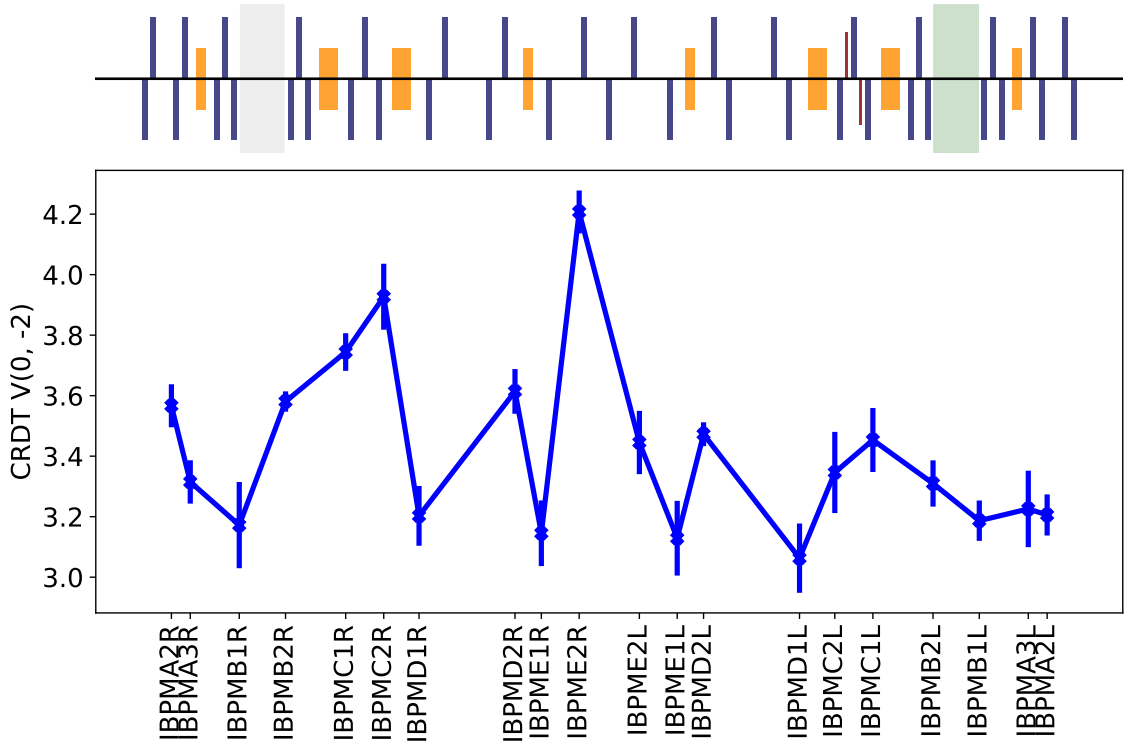

Figure 20: Measured skew sextupole C-RDT at a working point of $Q_x = 5.28$, $Q_y = 5.31$ and using only sextupoles in the left hand straight section for chromaticity correction.

C-RDT, while the amplitude of the C-RDT remains the same between the measurements, the evolution of the C-RDT is different between the two measurements. Given that hardware interventions on the octupole string took place in between the measurements shifts, future studies using the data corrected for the decoherence may thus look into potential effects of these interventions on the origin of the octupole line and linking it to specific measures taken.

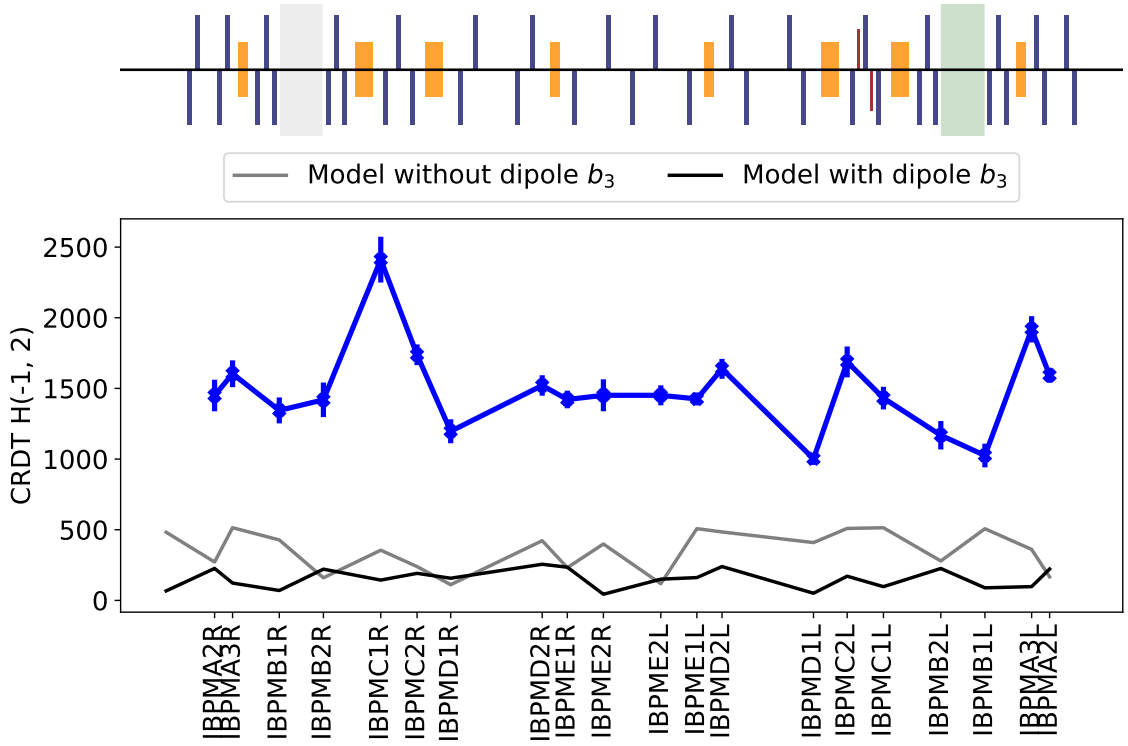

Figure 21: Measured octupole C-RDT at a working point of $Q_x = 5.28$, $Q_y = 5.31$ and using only sextupoles in the left hand straight section for chromaticity correction, together with a comparison to the expected model values.

Lastly, C-RDTs for measurements at the working point of $Q_x = 5.32$, $Q_y = 5.29$ are presented in Figs. 22-24. Results have been compared to the results at $Q_x = 5.325$, $Q_y = 5.29$, with no particular difference observed.

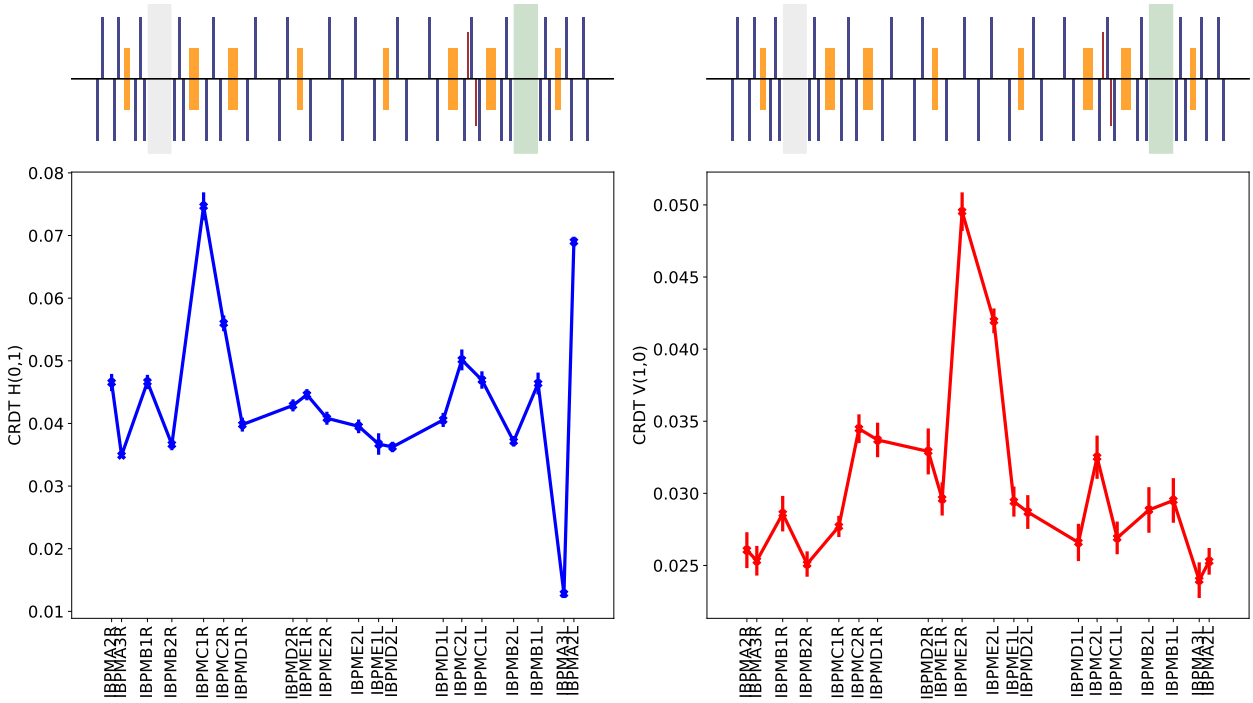

Figure 22: Measured coupling C-RDTs at a working point of $Q_x = 5.32$, $Q_y = 5.29$ and using only sextupoles in the left hand straight section for chromaticity correction.

Notably, a slight change in the structure pf the coupling C-RDTs is observed between the measurements for the working point of $Q_x = 5.28$, $Q_y = 5.31$ and at $Q_x = 5.32$, $Q_y = 5.29$. In particular, the change of the C-RDTs in the CR-straight section is noticeable, which could stem from a tilt of the quadrupoles used to achieve the tune change. In both cases a tune split of $\Delta Q = 0.03$ is used, and thus no significant change of the C-RDT amplitude is expected nor observed. Additionally, in this data sets no skew sextupole line is observed, which may be partly explained by Q_y further away from the $3Q_y$ resonance. For sextupole C-RDTs, a similar good qualitative agreement is observed between model and measurement as for the previous measurements. Although taken back to back, a change in the octupole C-RDT $H(-1, 2)$ is observed for the measurements at $Q_x = 5.28$, $Q_y = 5.31$ and at $Q_x = 5.32$, $Q_y = 5.29$, where in both cases only the sextupoles in the left hand straight section were powered. This change might then be explained by the change of the optics due to the tune knob, under assumption that the strength of any potential spurious octupole source has not changed between these measurements.

No analysis of resonance driving terms has been performed up until this point, as similarly to the C-RDT analysis, data has to be corrected for the decoherence first.

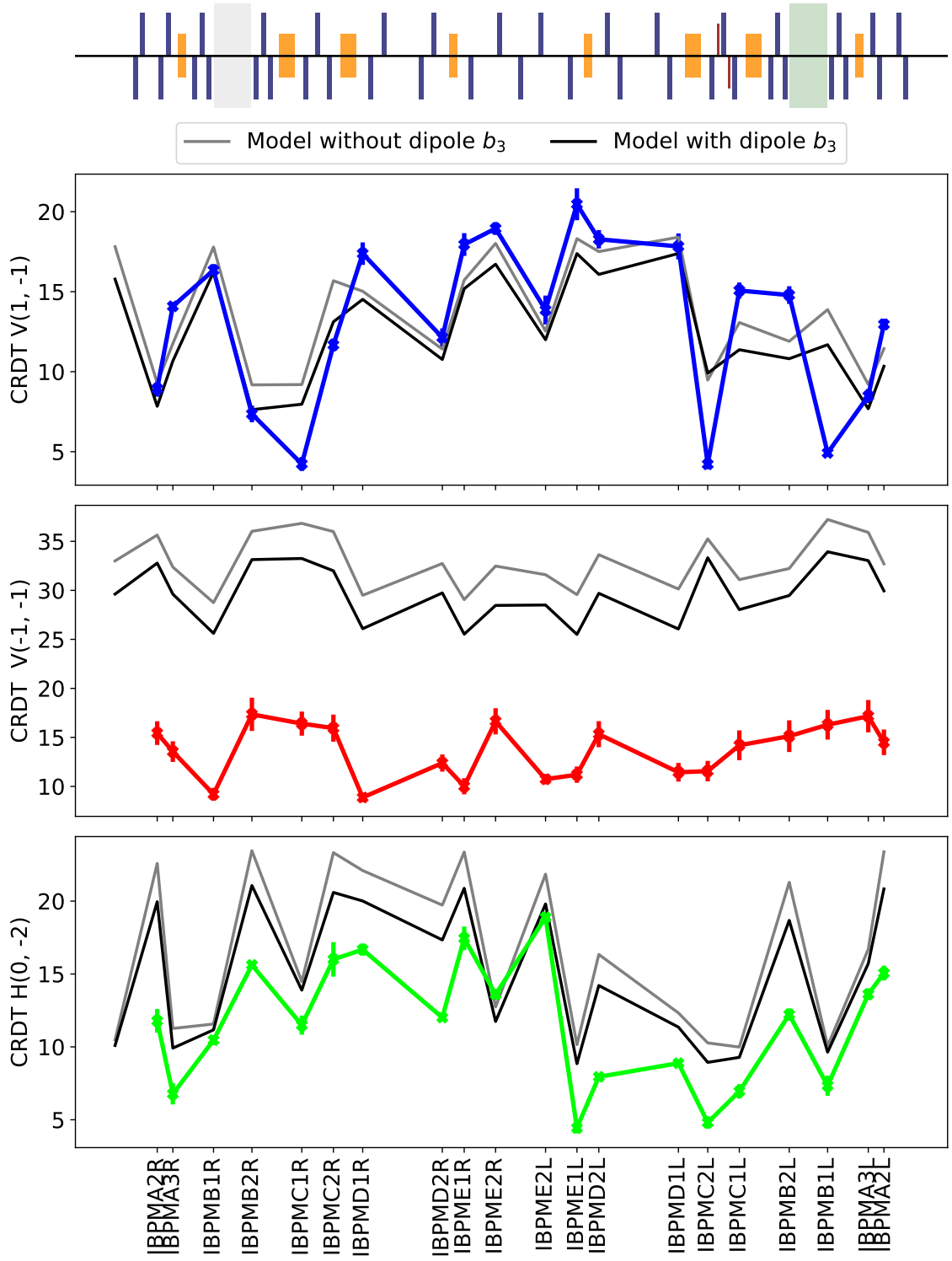

Figure 23: Measured sextupole C-RDTs at a working point of $Q_x = 5.32$, $Q_y = 5.29$ and using only sextupoles in the left hand straight section for chromaticity correction, together with a comparison to the expected model values.

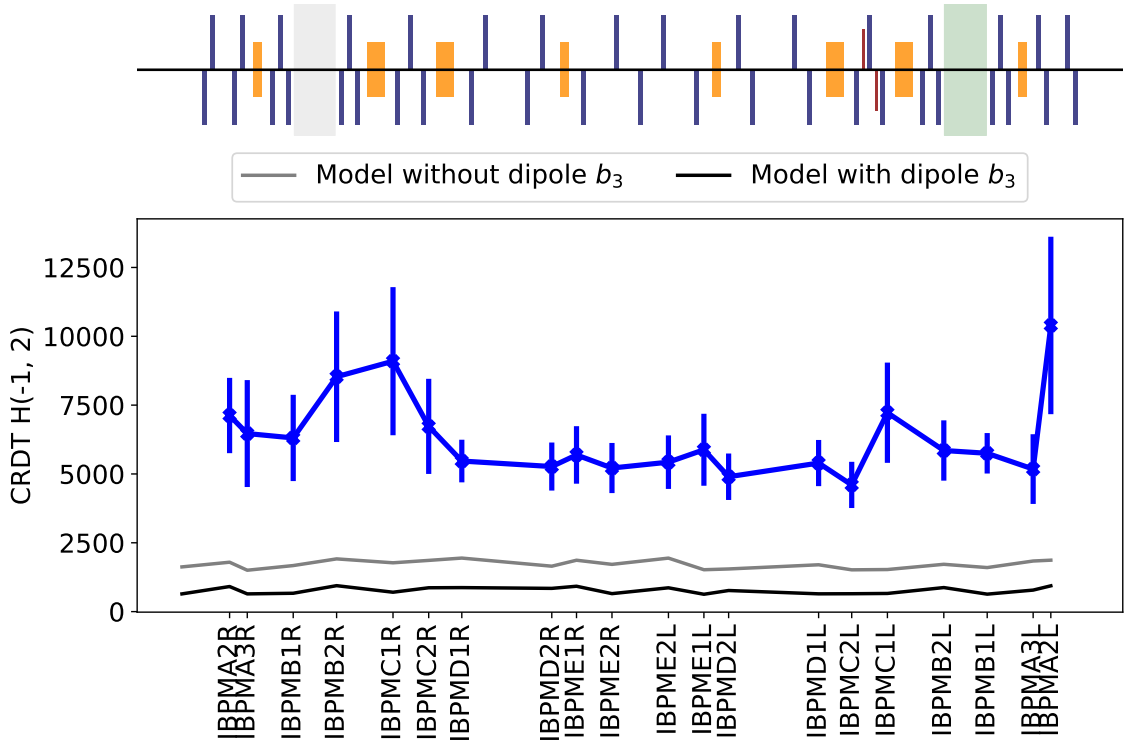

Figure 24: Measured octupole C-RDT at a working point of $Q_x = 5.32$, $Q_y = 5.29$ and using only sextupoles in the left hand straight section for chromaticity correction, together with a comparison to the expected model values.

5 Conclusions

Assessment of nonlinear magnetic fields, present either by design or by erroneous introduction, is one key task during the design and operation for many accelerators due to their potential performance limiting effects. One accelerator concept where this may be off particular importance is the recently proposed nonlinear integrable optics. It is based on introducing a nonlinear magnet with a particular potential which together with a special accelerator layout allows to generate an amplitude dependent tune shift, while not exciting any resonances. Other nonlinear fields in the accelerator may violate the required conditions and careful assessment is required to account for particle losses due to such sources. In this note, first studies on nonlinearities outside of the specific nonlinear channel have been presented for the case of the IOTA accelerator at Fermilab, one of the first machines built around the concept of nonlinear integrable optics. Using turn-by-turn data from the beam position monitors, acquired after an excitation with the kicker magnets, first a look in the linear optics is presented. Linear optics is in general well controlled in the IOTA accelerator, with a peak β-beating under 10 %. Following studies have looked into the amplitude detuning from the bare lattice without either the NL-magnet nor the octupole channel turned on. While initial measurements show discrepancies with the values expected from simulations, attributed to a spurious octupole source, measurements from a later shift show better agreement with the model values. The discrepancy is assumed to stem from hardware modification conducted before the first measurements, and no persistent spurious octupole source appears present in the IOTA-ring. Lastly, measurements of the combined resonance driving terms (C-RDT) have been presented for different working points and sextupole configurations. Good qualitative agreement for the sextupole C-RDTs has been observed between the model and measurements for the different configurations. Further studies are looking into the role of the decoherence of the specific spectral lines to account for the difference in amplitude between the model and measurements, to better compare between those and in view of a potential use to assess the location and strength of the nonlinear magnetic fields.

Acknowledgements

We would like to thank the FCC-project for providing funding to conduct the presented measurements. We would also like to thank the IOTA/FAST team for their hospitality, operational support, and advice. Lastly, we want to acknowledge the contributions of the members of the OMC-team at CERN through various discussions and help with the codes. This manuscript has been authored by Fermi Research Alliance, LLC under Contract No. DE-AC02-07CH11359 with the U.S. Department of Energy, Office of Science, Office of High Energy Physics.

References

[1] J. Bengtsson. 'The Sextupole Scheme for the Swiss Light Source (SLS): An Analytic Approach'. In: *SLS Note 9/97* (1997). URL: https://ados.web.psi.ch/slsnotes/sls0997.pdf.

[2] F. Pilat et al. 'Beam-Based Non-Linear Optics Corrections in Colliders'. In: *Proceedings of the 2005 Particle Accelerator Conference*. May 2005, pp. 601–605. DOI: 10.1109/PAC.2005.1590503.

[3] E. H. Maclean et al. 'First measurement and correction of nonlinear errors in the experimental insertions of the CERN Large Hadron Collider'. In: *Phys. Rev. ST Accel. Beams* 18 (12 Dec. 2015), p. 121002. DOI: 10.1103/PhysRevSTAB.18.121002. URL: https://link.aps.org/doi/10.1103/PhysRevSTAB.18.121002.

[4] F Bartolini R Schmidt. 'Normal form via tracking or beam data'. In: *Part. Accel.* 59.LHC-Project-Report-132. CERN-LHC-Project-Report-132 (Aug. 1997), 93–106. 10 p. URL: http://cds.cern.ch/record/333077.

[5] R Tomas-García. 'Direct Measurement of Resonance Driving Terms in the Super Proton Synchrotron (SPS) of CERN using Beam Position Monitors'. Presented on 30 Mar 2003. 2003. URL: https://cds.cern.ch/record/615164.

[6] V. Danilov and S. Nagaitsev. 'Nonlinear accelerator lattices with one and two analytic invariants'. In: *Phys. Rev. ST Accel. Beams* 13 (8 Aug. 2010), p. 084002. DOI: 10.1103/PhysRevSTAB.13.084002. URL: https://link.aps.org/doi/10.1103/PhysRevSTAB.13.084002.

[7] S. Antipov et al. 'IOTA (Integrable Optics Test Accelerator): facility and experimental beam physics program'. In: *Journal of Instrumentation* 12.03 (Mar. 2017), T03002–T03002. DOI: 10.1088/1748-0221/12/03/t03002. URL: https://doi.org/10.1088%2F1748-0221%2F12%2F03%2Ft03002.

[8] Stephen D. Webb et al. *Chromatic and Dispersive Effects in Nonlinear Integrable Optics*. 2015. arXiv: 1504.05981 [physics.acc-ph].

[9] S. Nagaitsev, A. Valishev and V. Danilov. 'Nonlinear Optics as a Path to High-Intensity Circular Machines'. In: *Proc. 46th ICFA Advanced Beam Dynamics Workshop on High-Intensity and High-Brightness Hadron Beams (HB10), Morschach, Switzerland, Sep.-Oct. 2010*, pp. 676–680.

[10] S. A. Antipov et al. 'Stripline Kicker for Integrable Optics Test Accelerator'. In: *Proc. 6th International Particle Accelerator Conference (IPAC'15), Richmond, VA, USA, May 3-8, 2015* (Richmond, VA, USA). International Particle Accelerator Conference 6. https://doi.org/10.18429/JACoW-IPAC2015-WEPTY051. Geneva, Switzerland: JACoW, June 2015, pp. 3390–3392. ISBN: 978-3-95450-168-7. DOI: https://doi.org/10.18429/JACoW-IPAC2015-WEPTY051. URL: http://jacow.org/ipac2015/papers/wepty051.pdf.

[11] A. Franchi et al. 'First simultaneous measurement of sextupolar and octupolar resonance driving terms in a circular accelerator from turn-by-turn beam position monitor data'. In: *Phys. Rev. ST Accel. Beams* 17 (7 July 2014), p. 074001. DOI: 10.1103/PhysRevSTAB.17.074001. URL: https://link.aps.org/doi/10.1103/PhysRevSTAB.17.074001.

[12] *Turn-by-turn data from the first NLOMC Shift*. https://cdcvs.fnal.gov/redmine/attachments/59363/NLOMC_Shift1_2020-03-02.zip.

[13] *Turn-by-turn data from the second NLOMC Shift*. https://cdcvs.fnal.gov/redmine/attachments/59363/NLOMC_Shift2_2020-03-04.zip.

[14] *Turn-by-turn data from the third NLOMC Shift*. https://cdcvs.fnal.gov/redmine/attachments/59363/NLOMC_Shift3_2020-03-07.zip.

[15] R.E. Meller et al. *Decoherence of Kicked Beams*. SSC-N-360. May 1987.

[16] *OMC3 Accelerator Optics Analysis Suite*. https://github.com/pylhc/omc3.

[17] *Beta-Beat Source*. https://github.com/pylhc/Beta-Beat.src.

[18] R. Calaga and R. Tomás. 'Statistical analysis of RHIC beam position monitors performance'. In: *Phys. Rev. ST Accel. Beams* 7 (4 Apr. 2004), p. 042801. DOI: 10.1103/PhysRevSTAB.7.042801. URL: https://link.aps.org/doi/10.1103/PhysRevSTAB.7.042801.

[19] E. Fol et al. 'Detection of faulty beam position monitors using unsupervised learning'. In: *Phys. Rev. Accel. Beams* 23 (10 Oct. 2020), p. 102805. DOI: 10.1103/PhysRevAccelBeams.23.102805. URL: https://link.aps.org/doi/10.1103/PhysRevAccelBeams.23.102805.

[20] A. Valishev et al. 'Beam Physics of Integrable Optics Test Accelerator at Fermilab'. In: *Proc. 3rd Int. Particle Accelerator Conf. (IPAC'12), New Orleans, LA, USA, May 2012*, pp. 1371–1373.

[21] A. L. Romanov. 'Testing of Advanced Technique for Linear Lattice and Closed Orbit Correction by Modeling Its Application for IOTA Ring at Fermilab'. In: *Proc. North American Particle Accelerator Conf. (NAPAC'16), Chicago, IL, USA, Oct. 2016*, pp. 1155–1157.

[22] A. Valishev on behalf of the IOTA collaboration. 'Fighting nonlinear dynamics with nonlinear elements'. In: *Mitigation Approaches for Storage Rings and Synchrotrons, ARIES-APEC workshop, GSI, June. 2020*. https://indico.gsi.de/event/10458/contributions/45017/attachments/31685/40147/2020-06-22_ARIES_APEC_Workshop.pdf.

[23] A. Langner and R. Tomás. 'Optics measurement algorithms and error analysis for the proton energy frontier'. In: *Phys. Rev. ST Accel. Beams* 18 (3 Mar. 2015), p. 031002. DOI: 10.1103/PhysRevSTAB.18.031002. URL: https://link.aps.org/doi/10.1103/PhysRevSTAB.18.031002.

[24] A. Wegscheider et al. 'Analytical N beam position monitor method'. In: *Phys. Rev. Accel. Beams* 20 (11 Nov. 2017), p. 111002. DOI: 10.1103/PhysRevAccelBeams.20.111002. URL: https://link.aps.org/doi/10.1103/PhysRevAccelBeams.20.111002.

[25] A. García-Tabarés Valdivieso and R. Tomás. 'Optics-measurement-based beam position monitor calibrations in the LHC insertion regions'. In: *Phys. Rev. Accel. Beams* 23 (4 Apr. 2020), p. 042801. DOI: 10.1103/PhysRevAccelBeams.23.042801. URL: https://link.aps.org/doi/10.1103/PhysRevAccelBeams.23.042801.

[26] A. Franchi et al. 'Vertical emittance reduction and preservation in electron storage rings via resonance driving terms correction'. In: *Phys. Rev. ST Accel. Beams* 14 (3 Mar. 2011), p. 034002. DOI: 10.1103/PhysRevSTAB.14.034002. URL: https://link.aps.org/doi/10.1103/PhysRevSTAB.14.034002.

[27] M. Hofer and R. Tomás. 'Effect of local linear coupling on linear and nonlinear observables in circular accelerators'. In: *Phys. Rev. Accel. Beams* 23 (9 Sept. 2020), p. 094001. DOI: 10.1103/PhysRevAccelBeams.23.094001. URL: https://link.aps.org/doi/10.1103/PhysRevAccelBeams.23.094001.